

Chapter 2

Fixed-Flux Model

Abstract In this chapter, the compressible, one-dimensional Two-Fluid Model (TFM) for stratified two-phase flow is introduced first. For conditions of practical interest, a characteristic analysis demonstrates that the acoustic roots are always real and that the origin of ill-posedness (or well-posedness) of the model lies in the material roots. Therefore, compressibility is neglected and an incompressible model is used to derive a reduced two-equation model by applying the fixed-flux approximation, which is the key to study the local material waves in isolation, and is referred to as the Fixed-Flux Model (FFM). It is demonstrated that the FFM reduces to the well-known Shallow Water Theory (SWT) under some conditions. While it is not possible to cover all the possible local instabilities for stratified flow with the FFM, we are interested in two significant cases: SWT and Kelvin–Helmholtz (KH) instabilities, otherwise known as kinematic and dynamic instabilities.

Furthermore, the local linear material stability analysis allows us to address the question of the ill-posed TFM, which is caused by the KH instability which also precisely differentiates the FFM from SWT. The dispersion analysis of the FFM shows the well known results that the hydrostatic force makes the TFM stable up to the KH instability and surface tension makes the unstable model well-posed beyond it (Ramshaw and Trapp, *Nuclear Science and Engineering*, 66, 93–102, 1978). However, the well-posed FFM is still Lyapunov unstable and a bounding nonlinear viscous mechanism will be analyzed in Chap. 4, in terms of SWT material shocks (Whitham, *Linear and Nonlinear Waves*, Wiley, New York, 1974). Finally, the numerical stability and convergence of a few finite-difference schemes typically used to simulate TFM problems is also addressed with the von Neumann stability analysis of the FFM.

2.1 Introduction

Gidaspow (1974) was the first to perform a characteristic analysis of the incompressible potential flow Two-Fluid Model (TFM) and demonstrate that the problem is ill-posed. Furthermore, for compressible flow a characteristic analysis demonstrates that the acoustic roots are always real and that the origin of an ill-posed TFM lies in the material roots.

First the compressible, one-dimensional characteristics for stratified two-phase flow are presented. Then an incompressible TFM is used to derive a reduced two-equation model by applying the fixed-flux approximation, which is the key to study the local material waves in isolation. Furthermore, the simplified Fixed-Flux Model (FFM) reduces to the well-known Shallow Water Theory (SWT) under some conditions.

Horizontal stratified wavy flows are among the simplest topologies of two-phase flows. Waves on oceans and rivers are some of the earliest phenomena analyzed and there is a wide body of literature. They are a good starting point to analyze the local stability of the TFM material waves. While we do not intend to cover all the possible local instabilities, encountered in stratified flows, which include several possible variations of the Orr–Sommerfeld equations (Barmak et al. 2016) as well as heat and mass transfer instabilities, we are interested in two significant fluid dynamics cases: SWT and Kelvin–Helmholtz (KH) instabilities, otherwise known as kinematic and dynamic instabilities. A good discussion on the fundamentals of kinematic waves (also referred to as continuity waves) and dynamic waves, and the associated instabilities, may be found in Wallis (1969).

The local material stability analysis allows us to address the question of the ill-posed TFM. This arises from averaging that removes several short wavelength physical mechanisms and is most acute in the case of one-dimensional models. The issue may be stated in its simplest form as follows: once the FFM goes beyond the KH instability the problem is no longer hyperbolic; it may be ill-posed elliptic or it may be well-posed in which case it is parabolic–hyperbolic. Sometimes an ill-posed TFM is regularized by adding significant numerical diffusion in which case the parabolic behavior damps the instability, others by adding an artificial interfacial force that returns the TFM to hyperbolic, in which case there is no instability. Therefore, the effect of regularization is to modify the local linear dynamics of the TFM.

A central objective of this chapter is to obtain an exact definition of an ill-posed TFM. First of all, it is important to remark that the ill-posed condition is a linear stability concept, and in the present case it is limited to the KH instability. However, the KH instability is not sufficient to make the TFM ill-posed. In fact, the problem arises only when a TFM is not sufficiently complete, i.e., it is possible to have a well-posed unstable TFM with a judicious choice of short wavelength physical mechanisms that balance the KH force. In the case of horizontal stratified flows, some of these mechanisms were identified early on: the hydrostatic force that makes the model stable up to the KH instability and surface tension (Ramshaw and Trapp 1978) or viscosity (Arai 1980), which make the unstable model well-posed beyond it. However, the unstable well-posed TFM remains Lyapunov unstable or practically ill-posed (Drew and Passman 1999, chap. 20), a problem that is left for Chap. 4.

First a two-equation incompressible FFM is derived from the incompressible isothermal four-equation TFM for horizontal stratified-wavy flow. It is shown that, below the KH instability limit, it reduces exactly to SWT for small density ratios. Well-known linear stability analyses may be applied that are relevant to stable and kinematically unstable cases, i.e., characteristics and the dispersion relation. The results are consistent with the TFM linear stability analysis of Barnea and

Taitel (1993) who identified the kinematic instability for stratified two-phase flows and Brauner and Maron (1993) who improved the analysis by including the wave sheltering effect. Eventually, these analyses may be extended with the nonlinear analysis of SWT (Whitham 1974) to material shocks and expansion waves for stable and kinematically unstable cases.

Secondly, the stability of a few finite-difference numerical schemes is analyzed. The development of a numerical scheme is complicated by the difficulty to separate physical, nonphysical, and/or numerical instabilities. It is well known that a numerical scheme must satisfy the von Neumann stability condition. In particular, we require that any numerical scheme be stable for the shortest wavelengths that can be represented numerically, i.e., $2\Delta x$, otherwise the discretization noise would be amplified until it dominates the solution. The specific objective is to develop a second-order finite-difference scheme for a well-posed model to perform nonlinear simulations that are reasonably accurate.

However, when the TFM is ill-posed, as in several industrial codes, it becomes necessary to use a numerical method that has sufficient damping at short wavelengths to suppress the unstable tendencies of the differential model. That is why we also review first-order upwind numerical schemes that have significant numerical, i.e., artificial, viscosity.

2.2 Compressible Two-Fluid Model

2.2.1 One-Dimensional Model Equations

A wavespeed analysis for compressible two-phase flow is performed with a TFM that is similar to Wallis (1969) separated flow model, to demonstrate that the acoustic characteristics of the TFM are always real. This is done to demonstrate that the ill-posed behavior of the TFM is only associated with the material waves, which is the concern of the rest of the book. For the characteristic analysis we only need to consider a simplified version of the 1D TFM for stratified flow, cf. Appendix A.

Generally, the density is given by the pressure and temperature through an equation of state. Here, we take the isentropic case so that the density material derivatives for compressible flow may be written as:

$$\frac{D_k \rho_k}{Dt} \equiv \frac{\partial}{\partial t} \rho_k + u_k \frac{\partial}{\partial x} \rho_k = \frac{1}{c_k^2} \frac{D_k p_{2i}}{Dt}, \quad k = 1, 2. \quad (2.1)$$

To include compressibility the speed of sound, given by $c_k = \sqrt{\partial p_k / \partial \rho_k}$, is needed to derive the material derivative of the density for each phase, where it has been assumed that $p_k = p_{2i}$. Inserting this into the continuity equations yields

$$\frac{D_1 \alpha_1}{Dt} + \alpha_1 \frac{\partial u_1}{\partial x} + \frac{\alpha_1}{\rho_1 c_1^2} \frac{D_1 p}{Dt} = 0, \quad (2.2)$$

$$-\frac{D_2 \alpha_1}{Dt} + \alpha_2 \frac{\partial u_2}{\partial x} + \frac{\alpha_2}{\rho_2 c_2^2} \frac{D_2 p}{Dt} = 0. \quad (2.3)$$

The momentum equations for this simple TFM for stratified flow only include the hydrostatic force, i.e., first-order derivatives only,

$$\rho_1 \frac{D_1 u_1}{Dt} = -\frac{\partial p}{\partial x} + \rho_1 g_y H \frac{\partial \alpha_1}{\partial x}, \quad (2.4)$$

$$\rho_2 \frac{D_2 u_2}{Dt} = -\frac{\partial p}{\partial x} + \rho_2 g_y H \frac{\partial \alpha_1}{\partial x}, \quad (2.5)$$

where α , ρ , u , p , and c are the time and space-averaged void fraction, density, velocity, pressure, and sound speed. The momentum equations remain the same as those in Appendix A because they are nonconservative so there are no derivatives of the densities. The void fractions are related by $\alpha_1 + \alpha_2 = 1$ and $g_y H$ is the product of the transverse gravitational constant and the channel height (Fig. 2.3).

Of course the analysis of the compressible 1D TFM is much more extensive and only the simplest possible case is considered in this section. For a thorough up-to-date analysis of the gas dynamics aspects of the TFM the reader is referred to Stadtke (2006).

2.2.2 Characteristics

The characteristics analysis follows those of Gidaspow (1974) and Stadtke (2006). Expanding the derivatives in Eqs. (2.2)–(2.5), the original system of partial differential equations can be cast into vector equation form as:

$$\mathbf{A} \frac{d}{dt} \underline{\phi} + \mathbf{B} \frac{d}{dx} \underline{\phi} = \mathbf{0}, \quad (2.6)$$

where $\underline{\phi} = [\alpha_1, u_1, u_2, p]^T$ is the vector of the independent variables. The coefficient matrices, obtained from Eqs. (2.2)–(2.5), are as follows:

$$\mathbf{A} = \begin{bmatrix} 1 & 0 & 0 & \frac{\alpha_2}{\rho_2 c_2^2} \\ -1 & 0 & 0 & \frac{\alpha_1}{\rho_1 c_1^2} \\ 0 & \rho_2 & 0 & 0 \\ 0 & 0 & \rho_1 & 0 \end{bmatrix}, \quad (2.7)$$

$$\mathbf{B} = \begin{bmatrix} u_2 & \alpha_2 & 0 & \frac{\alpha_2 u_2}{\rho_2 c_2^2} \\ -u_1 & 0 & \alpha_1 & \frac{\alpha_1 u_1}{\rho_1 c_1^2} \\ -\frac{1}{2}\rho_2 gH & \rho_2 u_2 & 0 & 1 \\ -\frac{1}{2}\rho_1 gH & 0 & \rho_1 u_1 & 1 \end{bmatrix}. \quad (2.8)$$

This system of equations must satisfy $\det[\mathbf{B} - c\mathbf{A}] = 0$ for a nontrivial solution to exist. Neglecting the hydrostatic forces and making $u_1 = u_2 = 0$, the solutions are $c = 0, 0, +c_{2\phi}, -c_{2\phi}$, where the first two characteristics are the void wave speeds and the last two characteristics are the (isentropic) acoustic wave speeds:

$$c_{2\phi} = \sqrt{\frac{\frac{\alpha_2 \rho_1 + \alpha_1 \rho_2}{\alpha_2 \rho_1} + \frac{\alpha_1 \rho_2}{\alpha_1 \rho_2}}{\frac{c_1^2}{c_1^2} + \frac{c_2^2}{c_2^2}}}. \quad (2.9)$$

This is the well-known sound speed of stratified flow with no relative velocity (Wallis 1969).

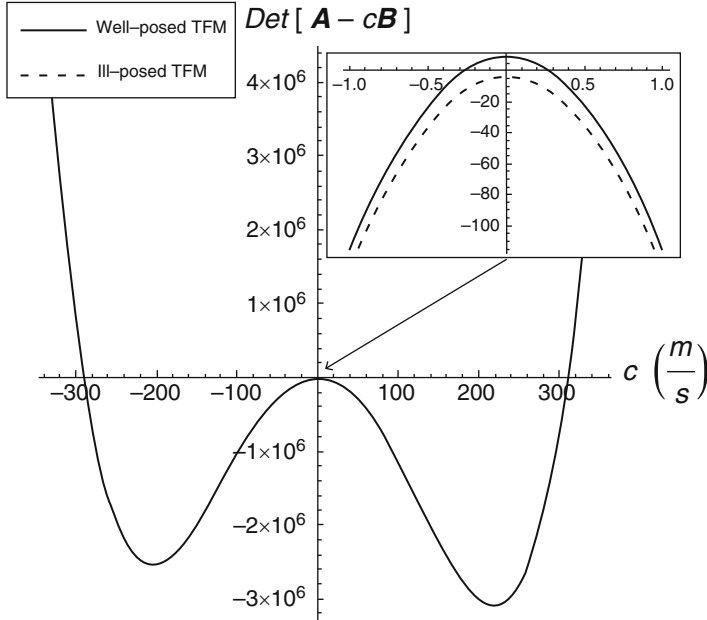


Fig. 2.1 Characteristic polynomial vs. wave speed

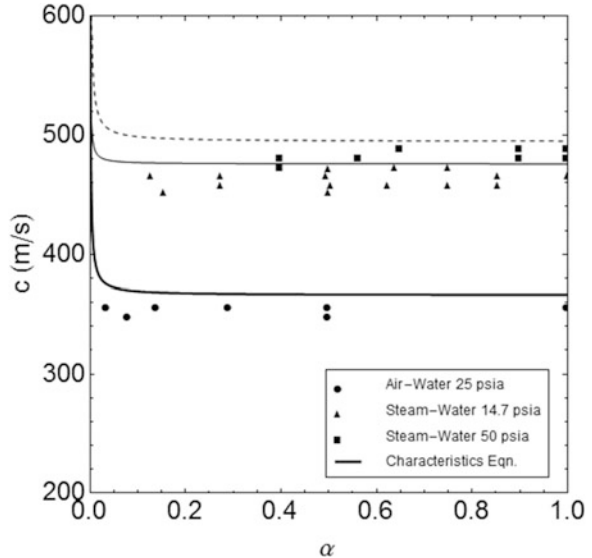
Of great significance to the present discussion is the characteristic polynomial including hydrostatic forces. Consider the full characteristic polynomial:

$$\det[\mathbf{A} - c\mathbf{B}] = \frac{1}{2} \alpha_1 \alpha_2 \left[\alpha_2 \rho_1 \left[\alpha_1 g H - 2(u_1 - c)^2 \right] + \frac{(u_2 - c)^2 \left\{ c_1^2 \left[2\alpha_2 \rho_1 (u_1 - c)^2 - \alpha_1 \rho_2 c_2^2 - \alpha_1 \alpha_2 \rho_1 g H \right] - 2\alpha_1 \rho_2 c_2^2 (u_1 - c)^2 \right\}}{c_1^2 c_2^2} \right] \quad (2.10)$$

which is plotted in Fig. 2.1 for the case of stratified air–water flow at atmospheric conditions: $\rho_1 = 1000 \text{ kg/m}^3$, $\rho_2 = 1 \text{ kg/m}^3$, $c_1 = 1500 \text{ m/s}$, $c_2 = 300 \text{ m/s}$, $\alpha = 0.5$, $u_1 = u_2 = 0$, and $H = 0.03 \text{ m}$. What is significant about this figure is that the characteristic equation, $\det[\mathbf{A} - c\mathbf{B}] = 0$, may have four or two real eigenvalues, depending on whether the system is well-posed or not. The two acoustic roots are approximately $\pm 300 \text{ m/s}$ and the material wave speeds are approximately $\pm 0.3 \text{ m/s}$. Figure 2.1 also shows a close-up of the origin where it is seen that when the gas velocity is increased from $u_2 = 0$ to 10 m/s the polynomial no longer intersects the x -axis, so the material wave speeds are now imaginary (i.e., ill-posed) because the KH criterion has been exceeded. On the other hand, the acoustic wave speeds are always real. Therefore, when compressibility is included, the 1D TFM is always acoustically hyperbolic, as the 1D Euler equations. It is the TFM material waves that differ, and this occurs only beyond the KH instability. This aspect of the TFM is different from the Euler equations and it is better described by a model for surface waves, i.e., the FFM that is related to SWT and is developed in the next section.

In order to validate the model, the largest characteristic value is compared to the data of Henry et al. (1971) in Fig. 2.2. The phase velocities are set for a horizontal

Fig. 2.2 Comparison of the sound speed model with the data of Henry et al. (1971)



pipe with $u_1 = 2$ m/s, $u_2 = 11$ m/s and $H = 0.05$ m. The graphic shows that the characteristic analysis compares well with the data. This comes as no surprise since the acoustic speed obtained with Eq. (2.6) matches the frozen separated sound speed model of Wallis (1969), which is known to work well for stratified flows.

Before moving on to an incompressible model it is worthy of note that industrial TFM codes with upwind first-order numerical schemes may predict acoustic waves quite accurately. The reason for this is that they have near second-order accuracy for acoustic propagation when the time step is sufficiently small so that the acoustic Courant number is significantly lower than unity (Tiselj 2000). This is necessary because these codes employ the pressure Poisson equation method which treats the pressure implicitly, cf. Sect. 3.4.3, and are prone to significant wave dispersion otherwise.

2.3 Incompressible Two-Fluid Model

2.3.1 One-Dimensional Model Equations

The analysis of the ill-posed TFM is performed with an incompressible model since it was previously established that the model acoustics are unconditionally well-posed and only the material waves render the system ill-posed. Therefore, the rest of the chapter, and the book, will be devoted to the analysis of the incompressible TFM so the analysis becomes simpler. The incompressible isothermal 1D TFM derived in Appendix A for horizontal stratified flow is a system of four partial differential equations (PDE). This model does not include compressibility but is otherwise more complete than Eqs. (2.2)–(2.5) because it includes additional terms for gravity, surface tension, and friction, some of which play a significant role in the stability of the model. Another simplification is that the velocity distribution parameters, i.e., shape factors, are assumed to be unity corresponding to uniform velocity profiles. This constraint will be removed in Chap. 4. Finally the viscous terms have been left out. The conservation of mass and momentum equations (A.22) to (A.25) applied to the flow between two parallel plates and excluding the viscous terms reduce to,

$$\boxed{\frac{D_1 \alpha_1}{Dt} + \alpha_1 \frac{\partial u_1}{\partial x} = 0,} \quad (2.11)$$

$$\boxed{-\frac{D_2 \alpha_1}{Dt} + \alpha_2 \frac{\partial u_2}{\partial x} = 0,} \quad (2.12)$$

$$\rho_1 \frac{D_1 u_1}{Dt} = -\frac{\partial p_{2i}}{\partial x} - \rho_1 g_y H \frac{\partial \alpha_1}{\partial x} + \sigma H \frac{\partial^3 \alpha_1}{\partial x^3} + \rho_1 g_x + \frac{1}{\alpha_1 H} \frac{f_i}{2} \rho_2 (u_2 - u_1)^2 - \frac{1}{\alpha_1 H} \frac{f_1}{2} \rho_1 |u_1| u_1, \quad (2.13)$$

$$\rho_2 \frac{D_2 u_2}{Dt} = -\frac{\partial p_{2i}}{\partial x} + \rho_2 g_y H \frac{\partial \alpha_2}{\partial x} + \rho_2 g_x - \frac{1}{\alpha_2 H} \frac{f_i}{2} \rho_2 (u_2 - u_1)^2 - \frac{1}{\alpha_2 H} \frac{f_2}{2} \rho_2 |u_2| u_2, \quad (2.14)$$

where α_k , ρ_k , u_k , and p_{2i} are the averaged void fractions, densities, velocities, and the lighter phase interfacial pressure, respectively. The subscripts $k = 1, 2$ indicate the heavier and lighter phases respectively, as shown in Fig. 2.3. The void fractions are related by the total void fraction condition, $\alpha_1 + \alpha_2 = 1$, and the remaining parameters, g , H , and σ , are gravity, channel height, and surface tension. The coefficients f_1, f_2 , and f_i are the phasic wall and interfacial Fanning friction factors, respectively.

The first term on the RHS of the momentum equations is the pressure gradient. The next term is the hydrostatic force which is derived in Appendix A. In any industrial 1D TFM code the phasic pressures are assumed to be in equilibrium and the terms appearing in Eqs. 2.13 and 2.14 are the area averaged pressure whereas here it is assumed that the phases have distinct pressures that are related to a reference pressure with contributions from hydrostatic and surface tension forces. This is illustrated in Fig. 2.3. The effect of surface tension on the TFM was first analyzed in the open literature by Ramshaw and Trapp (1978), and it renders the model well-posed when KH is unstable.

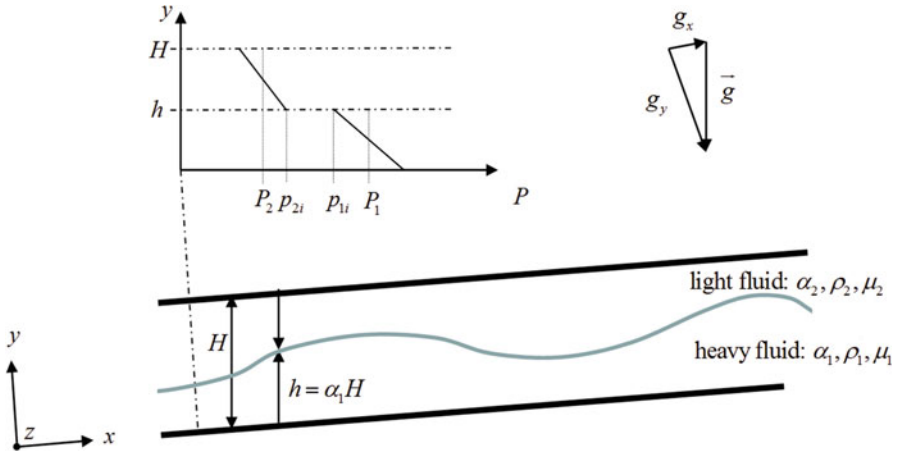


Fig. 2.3 Geometry and transverse pressure distribution for inclined channel flow, reprinted from Lopez de Bertodano et al. (2013), with permission from Begell House

2.3.2 Derivation of the Fixed-Flux Model

In spite of the simplifications made to derive the four PDEs of the previous section, they still present a formidable mathematical problem, even with the incompressible and isothermal assumptions. In this section, we make the additional fixed flux assumption and proceed to reduce the model to two PDEs following the approach of Holmås et al. (2008). Upon the further assumption of low density ratio the model may be simplified even more into the Shallow Water Theory (SWT) equations which have been the object of significant nonlinear stability research by Whitham (1974) among many others. The present derivation follows that by Lopez de Bertodano et al. (2013).

The first PDE is the sum of the two continuity Eqs. (2.11) and (2.12):

$$\frac{\partial}{\partial t}(\rho_1\alpha_1 + \rho_2\alpha_2) + \frac{\partial}{\partial x}(\rho_1\alpha_1u_1 + \rho_2\alpha_2u_2) = 0. \quad (2.15)$$

The second equation is the difference of the two momentum Eqs. (2.13) and (2.14), which eliminates the pressure:

$$\begin{aligned} \frac{\partial}{\partial t}(\rho_1u_1 - \rho_2u_2) + \frac{\partial}{\partial x}\left(\frac{1}{2}\rho_1u_1^2 - \frac{1}{2}\rho_2u_2^2 + (\rho_1 - \rho_2)g_yH\alpha_1\right) - \sigma H \frac{\partial^3\alpha_1}{\partial x^3} \\ = (\rho_1 - \rho_2)g_x - \frac{1}{\alpha_1H}\frac{f_1}{2}\rho_1u_1^2 + \frac{1}{\alpha_2H}\frac{f_2}{2}\rho_2u_2^2 + \left(\frac{1}{\alpha_1H} + \frac{1}{\alpha_2H}\right)\frac{f_i}{2}\rho_2(u_2 - u_1)^2. \end{aligned} \quad (2.16)$$

It is significant that the momentum equations are subtracted in this model because this links the local instabilities in some sense to the relative velocity. Two more equations are needed for closure. The first is the void fraction condition

$$\alpha_1 + \alpha_2 = 1 \quad (2.17)$$

and the second is the volumetric flux condition obtained from the time derivative of the void fraction condition combined with the continuity equations:

$$\frac{\partial}{\partial t}(\alpha_1 + \alpha_2) + \frac{\partial j}{\partial x} = 0, \quad (2.18)$$

where $j = \alpha_1u_1 + \alpha_2u_2$ is the total volume flux which, taking into account Eq. (2.17), ends up being a function only of time. We will further assume it to be constant in time so $j(x, t) = \text{constant}$. This is the fundamental fixed flux assumption which greatly simplifies the TFM equations because it replaces the momentum PDE of the mixture, corresponding to the sum of the TFM momentum equations, with an algebraic equation. By doing so, it restricts the model from an engineering perspective. Furthermore, it removes the very long wave system instabilities, due to the dynamics of the total flux like flow excursions and density wave oscillations, but it

preserves the local instabilities. The advantage for our purposes is that the single resulting momentum equation corresponds to the dynamics of the relative velocity which cause the TFM to be ill-posed.

We now follow the procedure of Holmås (2008) to recast this model in terms of the original variables $\underline{\phi} = [\alpha_1, u_1]^T$. First, Eqs. (2.15) and (2.16) are rewritten in matrix form, namely:

$$\frac{\partial}{\partial t} \underline{\psi} + \frac{\partial}{\partial x} \underline{\varphi} + \mathbf{E} \frac{\partial^3}{\partial x^3} \underline{\phi} = \underline{\xi}, \quad (2.19)$$

where

$$\underline{\psi} = \begin{bmatrix} \rho_1 \alpha_1 + \rho_2 \alpha_2 \\ \rho_1 u_1 - \rho_2 u_2 \end{bmatrix}, \quad \underline{\varphi} = \begin{bmatrix} \rho_1 \alpha_1 u_1 + \rho_2 \alpha_2 u_2 \\ \frac{1}{2} \rho_1 u_1^2 - \frac{1}{2} \rho_2 u_2^2 + (\rho_1 - \rho_2) g_y H \alpha_1 \end{bmatrix}, \quad \mathbf{E} = \begin{bmatrix} 0 & 0 \\ -\sigma H & 0 \end{bmatrix} \quad (2.20)$$

and the source terms are given by

$$\underline{\xi} = \begin{bmatrix} 0 \\ (\rho_1 - \rho_2) g_x - \frac{1}{\alpha_1 H} \frac{f_1}{2} \rho_1 u_1^2 + \frac{1}{\alpha_2 H} \frac{f_2}{2} \rho_2 u_2^2 + \left(\frac{1}{\alpha_1 H} + \frac{1}{\alpha_2 H} \right) \frac{f_i}{2} \rho_2 (u_2 - u_1)^2 \end{bmatrix}. \quad (2.21)$$

The next step is to convert this system of equations into primitive variables

$$\mathbf{A} \frac{\partial}{\partial t} \underline{\phi} + \mathbf{B} \frac{\partial}{\partial x} \underline{\phi} + \mathbf{E}' \frac{\partial^3}{\partial x^3} \underline{\phi} = \underline{F}, \quad (2.22)$$

where, applying the chain rule,

$$\mathbf{A} = \mathbf{I}, \quad \mathbf{B} = \left[\frac{\partial \underline{\psi}}{\partial \underline{\phi}} \right]^{-1} \frac{\partial \underline{\varphi}}{\partial \underline{\phi}}, \quad \mathbf{E}' = \left[\frac{\partial \underline{\psi}}{\partial \underline{\phi}} \right]^{-1} \mathbf{E}, \quad \underline{F} = \left[\frac{\partial \underline{\psi}}{\partial \underline{\phi}} \right]^{-1} \underline{\xi}.$$

The matrices $\frac{\partial \underline{\psi}}{\partial \underline{\phi}}$ and $\frac{\partial \underline{\varphi}}{\partial \underline{\phi}}$ of the chain rule derivatives are obtained using the void fraction condition, Eq. (2.17), and the volumetric flux condition, $j = \text{constant}$, such that:

$$\begin{aligned} \frac{\partial \underline{\psi}}{\partial \underline{\phi}} &= \begin{bmatrix} \rho_1 - \rho_2 & 0 \\ -\frac{\rho_2(j - u_1)}{\alpha^2} & \rho_1 + \frac{(1 - \alpha)\rho_2}{\alpha} \end{bmatrix} \rightarrow \left[\frac{\partial \underline{\psi}}{\partial \underline{\phi}} \right]^{-1} \\ &= \begin{bmatrix} \frac{1}{\rho_1 - \rho_2} & 0 \\ \frac{\rho_2(j - u_1)}{\alpha(\rho_1 - \rho_2)(\alpha(\rho_1 - \rho_2) + \rho_2)} & \frac{\alpha}{\alpha(\rho_1 - \rho_2) + \rho_2} \end{bmatrix} \end{aligned} \quad (2.23)$$

and

$$\frac{\partial \varphi}{\partial \underline{\phi}} = \left[\frac{g_y H \alpha^3 (\rho_1 - \rho_2) - \rho_2 (j - u_1) (j - u_1 (1 - \alpha))}{\alpha^3} \quad \rho_1 u_1 + \frac{\rho_2 (1 - \alpha) (j - u_1 (1 - \alpha))}{\alpha^2} \right]. \quad (2.24)$$

From these equations it is possible to obtain the elements of matrix \mathbf{B} :

$$B_{11} = u_1, \quad (2.25)$$

$$B_{12} = \alpha_1, \quad (2.26)$$

$$B_{21} = \frac{(1 - r_\rho)(1 - \alpha_1)g_y H - r_\rho(u_2 - u_1)^2}{1 - \alpha_1 + \alpha_1 r_\rho}, \quad (2.27)$$

$$B_{22} = \frac{(1 - \alpha_1)u_1 + r_\rho \alpha_1 (2u_2 - u_1)}{1 - \alpha_1 + \alpha_1 r_\rho}. \quad (2.28)$$

For further simplification it is convenient to perform a Taylor series expansion of these elements in terms of the density ratio, $r_\rho = \rho_2/\rho_1$. Thus:

$$B_{21} = g_y H - \frac{(u_2 - u_1)^2}{1 - \alpha_1} r_\rho + O(r_\rho^2), \quad (2.29)$$

$$B_{22} = u_1 + \frac{\alpha_1}{(1 - \alpha_1)} (2u_2 - u_1) r_\rho + O(r_\rho^2). \quad (2.30)$$

It is now assumed that $r_\rho \ll 1$, e.g., air water flows at atmospheric conditions, so the term of order r_ρ in B_{22} is neglected. In turn, the term proportional to r_ρ in B_{21} is preserved because we are interested in the Kelvin–Helmholtz instability, i.e., $r_\rho \frac{(u_2 - u_1)^2}{1 - \alpha_1} > g_y H$. The low density ratio assumption will be removed in Chap. 4, where the FFM consisting of Eqs. (2.27) and (2.28) will be used, but for this introductory chapter it is convenient to work with the simplified matrix \mathbf{B} :

$$\mathbf{B} \cong \begin{bmatrix} u_1 & \alpha_1 \\ g_y H - \frac{r_\rho (u_2 - u_1)^2}{1 - \alpha_1} & u_1 \end{bmatrix}. \quad (2.31)$$

Finally, the surface-tension tensor is $\mathbf{E}' \cong \frac{1}{\rho_1} \mathbf{E}$, and the simplified source terms become

$$\underline{F} = \begin{bmatrix} 0 \\ F \end{bmatrix} \cong \begin{bmatrix} 0 \\ g_x - \frac{1}{\alpha_1 H} \frac{f_1}{2} u_1^2 + \frac{1}{\alpha_2 H} \frac{f_2}{2} r_\rho u_2^2 + \left(\frac{1}{\alpha_1 H} + \frac{1}{\alpha_2 H} \right) \frac{f_i}{2} r_\rho (u_2 - u_1)^2 \end{bmatrix}. \quad (2.32)$$

Therefore, the FFM may now be written in the familiar SWT form, including surface tension which is not usual but is needed for the following stability analysis,

$$\boxed{\frac{\partial \alpha_1}{\partial t} + u_1 \frac{\partial \alpha_1}{\partial x} + \alpha_1 \frac{\partial u_1}{\partial x} = 0,} \quad (2.33)$$

$$\boxed{\frac{\partial u_1}{\partial t} + u_1 \frac{\partial u_1}{\partial x} - C \frac{\partial \alpha_1}{\partial x} = \frac{\sigma H}{\rho_1} \frac{\partial^3 \alpha_1}{\partial x^3} + F,} \quad (2.34)$$

where

$$\boxed{C = r_p \frac{(u_2 - u_1)^2}{1 - \alpha_1} - g_y H.} \quad (2.35)$$

If C is negative and surface tension is neglected the two-equation model becomes the well-known 1D SWT equations. Furthermore, $C = 0$ is the approximate Kelvin–Helmholtz criterion, given by Eq. (2.147) in Ishii and Hibiki (2006), in the limit $r_p \rightarrow 0$:

$$(u_2 - u_1)^2 > \frac{1 - \alpha_1}{r_p} g_y H. \quad (2.36)$$

Therefore, if C is positive Eqs. (2.33) and (2.34) represent the KH unstable case which is no longer considered SWT, i.e., it is unique to the TFM. It is now possible to define the types of TFM waves and instabilities that will be analyzed in this chapter.

Following Wallis, kinematic waves are associated to the kinematic condition, i.e., $F(\alpha_1, u_1) = 0$, where the kinematic wave speed derived in Appendix B.5.1, is given by $v_w = -\alpha_1 \frac{\partial F / \partial \alpha_1}{\partial F / \partial u_1}$. If the KH condition is satisfied then dynamic waves

occur with wave speed, derived also in Appendix B.5.1, given by $c = \sqrt{-\alpha_1 C}$. The respective instability conditions are $v_w > c$ and $C > 0$. The first, associated with kinematic waves, is referred to as the SWT instability in this book. The second, associated with dynamic KH waves, is the KH instability. These are the viscous and inviscid Kelvin–Helmholtz instabilities of Barnea and Taitel (1993). In section 2.4.2 it will be shown that the SWT instability occurs at lower flows than the KH instability. Because of the similarity between the FFM Eqs. (2.33) and (2.34) and SWT the linear and nonlinear behavior of the stable and kinematically unstable FFM (i.e., $C < 0$) may be understood in terms of SWT, e.g., Whitham (1974). If $C = 0$ and $F = 0$ the system becomes the Water Faucet Problem of Sect. 2.7 (Ransom 1984) which has been used for the verification of the TFM in nuclear reactor safety codes. The case $C > 0$ corresponds to the KH unstable TFM and is relevant for the analysis of two-phase flow in general and industrial codes in particular. However, the nonlinear behavior of the KH unstable TFM has not

been explored beyond the pioneering mathematical analyses of Keyfitz et al. (2004) and Kreiss and Yström (2002). In this chapter, these works are extended to the physically relevant case of stratified two-phase flow.

It cannot be stressed too much that the present analysis for local instabilities is based on the fixed flux approximation. This approximation is removed in Chap. 6 where global instabilities will be analyzed with the Drift-Flux Model. It is remarkable that the kinematic assumption, used instead to derive the DFM, removes the local instabilities.

2.4 Linear Stability

2.4.1 Dispersion Relation for the Kelvin–Helmholtz Instability ($F = 0$)

Up to this point, we have reduced the TFM to a set of two equations for two material waves, which are remarkable similar to the equations of the SWT. The fact that the FFM resembles SWT is a major benefit because of the large body of existing work on the analysis of surface waves with SWT. We consider first the Kelvin–Helmholtz instability shown schematically in Fig. 2.4. The KH instability is defined in the strict sense of Section 4 of Drazin and Reid (1981) as a transverse discontinuity in the velocity which only occurs at a vortex sheet or a vortex line for single-phase flow and is ill-posed for inviscid flow. We should distinguish between the latter and the shear layer instability, which in classical fluid mechanics is usually referred to as the KH instability, where the velocity changes across a finite width and which is not ill-posed. This is the central issue, namely, the fundamental problem of the TFM is that the KH instability occurs throughout the whole flow field at all times unless the velocities of the two phases are equal. For single-phase flow, on the other hand, the KH instability is sustainable only in inviscid flow since viscosity turns the vortex sheet into a shear layer immediately. Of course for two-phase flow there is also an abrupt change in the density but that is not the source of the ill-posed condition.

Artificial and physical viscous terms are now added to Eqs. (2.33) and (2.34), respectively, in an ad hoc approximate manner. A more rigorous treatment is left for Chap. 4. While kinematic viscosity is a legitimate part of the TFM momentum equations, artificial viscosity in the continuity equation is not. However, it is

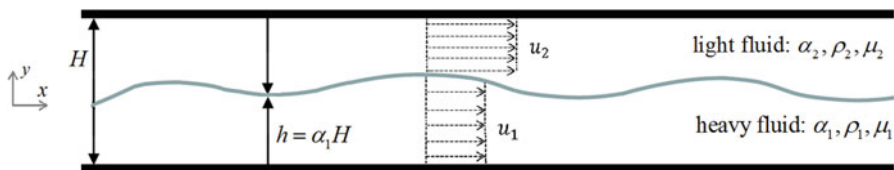


Fig. 2.4 Two-phase Kelvin–Helmholtz instability

included in this model because it is analogous to numerical viscosity often included in industrial codes to deal with the ill-posedness problem, and has a significant impact on the model stability. With these terms Eqs. (2.33) and (2.34) now become:

$$\frac{\partial \alpha_1}{\partial t} + u_1 \frac{\partial \alpha_1}{\partial x} + \alpha_1 \frac{\partial u_1}{\partial x} = \varepsilon \frac{\partial^2 \alpha_1}{\partial x^2}, \quad (2.37)$$

$$\frac{\partial u_1}{\partial t} + u_1 \frac{\partial u_1}{\partial x} - C \frac{\partial \alpha_1}{\partial x} = \nu \frac{\partial^2 u_1}{\partial x^2} + \frac{\sigma H}{\rho_1} \frac{\partial^3 \alpha_1}{\partial x^3} + F. \quad (2.38)$$

The viscous term in the momentum equation may include both physical and artificial viscosity.

We consider first the model with no friction terms, i.e., $F = 0$. The analysis follows that of Lopez de Bertodano et al. (2013). The two Eqs. (2.37) and (2.38) can be written as:

$$\mathbf{A} \frac{\partial}{\partial t} \underline{\phi} + \mathbf{B} \frac{\partial}{\partial x} \underline{\phi} + \mathbf{D} \frac{\partial^2}{\partial x^2} \underline{\phi} + \mathbf{E} \frac{\partial^3}{\partial x^3} \underline{\phi} = 0, \quad (2.39)$$

where $\underline{\phi} = [\alpha, u]^T$ is written dropping the subscripts such that $u = u_1$ and $\alpha = \alpha_1$. The matrix \mathbf{D} , which includes artificial and physical viscous terms in the continuity and momentum equations, is:

$$\mathbf{D} = \begin{bmatrix} -\varepsilon & 0 \\ 0 & -\nu \end{bmatrix}. \quad (2.40)$$

The characteristics, cf. Appendix B.2.2, given by the condition $\det[\mathbf{B} - c\mathbf{A}] = 0$ describe the behavior of the inviscid system such that:

$$\begin{aligned} C < 0 : c &= u \pm \sqrt{|C|\alpha}, \\ C = 0 : c &= u, \\ C > 0 : c &= u \pm i\sqrt{|C|\alpha}. \end{aligned}$$

The first two cases are well-posed or hyperbolic and well understood. However, the last case is ill-posed elliptic, which leads to difficulties (Barnea and Taitel 1993) and will be analyzed next with a dispersion analysis.

The dispersion relation extends the results of the characteristic analysis at zero wavelength to the full spectrum of wavelengths as described in Appendix B.2.2. The analysis of Appendix B.5.1 is reproduced here, only now $F = 0$, but the effects of viscosity and surface tension are included. The first step is to linearize the two-equation system using $\underline{\phi} = \underline{\phi}_0 + \underline{\phi}'$ and keeping only first-order terms with respect to $\underline{\phi}'$. Then a Fourier solution is applied $\underline{\phi}' = \hat{\underline{\phi}}' e^{i(kx - \omega t)}$ to the linearized equations, where k and ω are the wavenumber and the angular frequency. The solution must satisfy:

$$\det \left[-i\omega \mathbf{A} + ik\mathbf{B} + (ik)^2 \mathbf{D} + (ik)^3 \mathbf{E}' \right] = 0 \quad (2.41)$$

in order to have a nontrivial solution. The dispersion relation is:

$$\omega = uk - \frac{i}{2}(\varepsilon + \nu)k^2 \pm k \sqrt{-C\alpha - \left[\frac{1}{4}(\varepsilon - \nu)^2 - \frac{\sigma}{\rho_1} \alpha H \right] k^2}. \quad (2.42)$$

The material wave speed is then given by $c_w = \omega/k$:

$$c_w = u - \frac{i}{2}(\varepsilon + \nu)k \pm \sqrt{-C\alpha - \left[\frac{1}{4}(\varepsilon - \nu)^2 - \frac{\sigma}{\rho_1} \alpha H \right] k^2}. \quad (2.43)$$

For the inviscid case with no surface tension the wave speeds reduce to the characteristics, which are independent of wavelength. However, if there is viscosity or surface tension, different wavelengths travel at different wave speeds, i.e., the model becomes diffusive or dispersive. The critical point and the maximum growth rate (i.e., the most dangerous wave) may be obtained from $\omega_i = 0$ and $\frac{\partial \omega_i}{\partial k} = 0$, respectively. For the case where the viscosities are negligible the cut-off wavenumber reduces to $\sqrt{\frac{\rho_1 C}{\sigma H}}$ and the most dangerous wavenumber is

$$k_{\max} = \sqrt{\frac{\rho_1 C}{2\sigma H}} \quad (2.44)$$

with a corresponding wave growth rate,

$$\omega_{i, \max} = \sqrt{-\frac{\alpha \rho_1 C^2}{\sigma H}}. \quad (2.45)$$

It is worth mentioning that when the sign of g is reversed and $u_1 = u_2 = 0$ the 1D theory also predicts the critical Taylor wavenumber correctly and Eq. (2.44) predicts the most dangerous Taylor wavenumber within a factor of $\sqrt{2/3}$.

The KH stable case (i.e., $C \leq 0$) is valid up to gas speeds below the KH limit. The wave speeds in the limit of very small wavelengths (i.e., $k=0$) are the characteristic speeds given by Eq. (2.43), which are real, so the stable model is hyperbolic. Hyperbolicity is an attribute of well-posed stable wave propagation models, cf. Appendix B.2.2. Stable waves propagate at the characteristic speeds but do not grow.

The inviscid Eqs. (2.37) and (2.38) without surface tension are the well-known SWT equations with linear stability characteristics that are very simple. However, the nonlinear behavior leads to material shocks equivalent to those appearing in the

Burgers equation of Appendix B.3.1. We shall address this nonlinear behavior throughout the book.

The results for finite wavelengths retain this characteristic behavior, but the effects of viscosity and surface tension make the system dissipative and dispersive, respectively. If the short wave diffusion and dispersion are neglected then

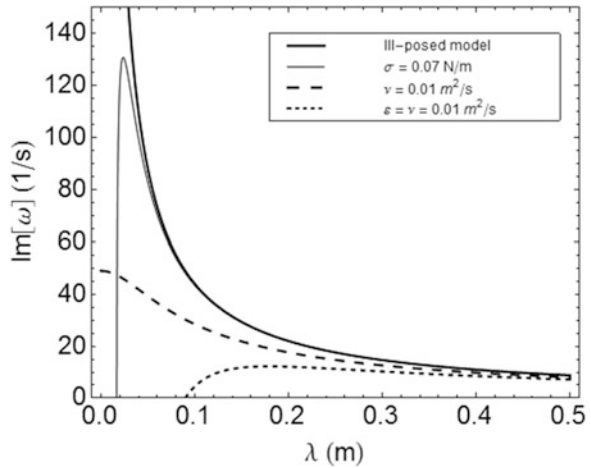
$$\frac{\omega}{k} = u \pm \sqrt{-C\alpha} \quad (2.46)$$

which is the equation for the characteristics.

The main difference between SWT and the FFM is that SWT does not account for the velocity of a second phase. Once the KH condition is exceeded this difference is fundamental. The dispersion analyses of the FFM including artificial viscosity, kinematic viscosity, and surface tension are shown in Fig. 2.5 for KH unstable conditions $H = 0.1$ m, $\alpha = 0.5$, $u_1 = 1$ m/s, $u_2 = 7$ m/s, $r_\rho = \frac{1}{50}$ and $\frac{\sigma H}{\rho_1} = 7 \times 10^{-6}$ m⁴/s². The basic, or Euler, 1D TFM is obtained from Eqs. (2.37) and (2.38) by setting $\varepsilon = \nu = 0$ and $\sigma = 0$. Beyond the KH limit the wave growth rates increase unboundedly as the wavelength shrinks to zero where there is a singularity. This singularity also occurs with the Euler equations but only for the case of the vortex sheet. The strict mathematical definition of ill-posedness is that at zero wavelength growth rate is infinite for any relative velocity other than zero. Furthermore, including wall and interfacial friction, even with unrealistically large coefficients values, the ill-posed nature of the dynamic instability at the zero wavelength does not change.

At this point of the analysis, it is relevant to compare the ill-posed TFM with the stability of the Euler and the Navier–Stokes equations of single-phase flow. First of all, both the 1D Euler equations and the 1D Navier–Stokes equations are not only

Fig. 2.5 Dispersion relation for FFM with $F = 0$, reprinted from Lopez de Bertodano et al. (2013), with permission from Begell House



well-posed but they are also stable. Furthermore, the multidimensional Euler vortex sheet is the only instance of an ill-posed single-phase flow problem (Drazin and Reid 1981), but it vanishes as soon as the shear-layer thickness becomes finite, i.e., the problem turns into an instability which is well-posed. Thus the Navier–Stokes equations are more physical in this sense because a vortex sheet becomes a shear layer immediately by the effect of viscosity, and so the problem is well-posed from the beginning. Therefore, the TFM has a unique condition compared to the Navier–Stokes equations because the averaging of the interfaces imprints the KH instability, i.e., the two distinct velocities that behave like an inherent and permanent vortex sheet. In this sense the ill-posed TFM question is relevant and the remedy will be pursued in this and further chapters adopting a variety of short wave physically stabilizing mechanisms that depend on the flow regime. Nevertheless, the linear growth rates of the well-posed models remain high. However, it is important to realize that the concern with the linear ill-posed issue of TFM stability goes too far sometimes, for it overshadows the more important issue of nonlinear stability. In the next two chapters it will be shown, with nonlinear simulations and analysis, that even when the initial growth rate of the waves is high a viscous mechanism stops the growth of the nonlinear waves.

The first such mechanism is surface tension. Figure 2.5 shows that it makes the model well-posed and introduces a cutoff wavelength. This cutoff wavelength is approximately 20 mm for this particular case of water–gas flow, i.e., $\sigma = 0.07$ N/m. Surface tension stabilization is the earliest published demonstration (Ramshaw and Trapp 1978) that the TFM may be rendered well-posed for unstable KH flow by including appropriate short wavelength physics. Nevertheless the maximum growth rate of the waves is high.

Furthermore Figure 2.5 shows that a very large kinematic viscosity of 0.01 m²/s, makes the model well-posed too but with no cutoff, i.e., the growth rate is maximum and large at zero wavelength, $\omega_i = \frac{aC}{\nu}$, which is unphysical and practically ill-posed.

Finally, industrial TFM codes are rendered well-posed adding numerical viscosity. Figure 2.5 shows the effect of a first-order upwind finite-difference discretization by arbitrarily setting a high artificial viscosity, $\varepsilon = \nu = 0.01$ m²/s. The artificial viscosity values were selected to obtain a cut-off wavelength of a representative pipe diameter, i.e., $D = 0.1$ m. In addition to being well-posed, the model now exhibits a cutoff wavelength for wave growth that sets a lower limit to the size of perturbations allowed to grow when the flow is unstable. The point of this exercise is that when the TFM is unstable, numerical viscosity makes it well posed. However, the cutoff wavelength may be arbitrarily adjusted changing the space and time discretizations. When the short wavelength components of the solution are not of interest, numerical regularization is often used, but it does not resolve the fundamental ill-posed behavior of the TFM in a physical sense and it precludes convergence beyond the KH criterion, as shall be demonstrated in Sect. 2.5.2.

The difference between an ill-posed TFM and an unstable one may now be addressed. It is clear from Fig. 2.5 that the TFM becomes ill-posed once the KH condition is exceeded. The physical reason in our case is that the averaging removes the interface with its shear layer, so it perpetuates the ill-posed KH condition, i.e., the vortex sheet, as opposed to the instability of the shear layer which is well-posed. Furthermore, it is well known that the TFM loses hyperbolicity in the process. However, the question remains: is the TFM unacceptable because it is not hyperbolic anymore? The answer depends on the choice of stabilization since the Fig. 2.5 also shows that the addition of short wave physics, in particular viscosity and surface tension for the purpose of this discussion, renders the model well-posed and, as we shall see when nonlinear stability is considered, well behaved. Furthermore, the physical mechanism that turns a vortex sheet into a shear layer in the Navier–Stokes equations is viscous diffusion, which is a parabolic process, and it is well known that the Navier–Stokes equations are hyperbolic–parabolic in addition to being well-posed. So a hyperbolic–parabolic viscous TFM should be a welcome alternative to an ill-posed model and preferable to a TFM that is artificially hyperbolic.

The next and more important question is whether a well-posed but unstable TFM is sufficient. Well-posedness, as defined in this section, is a linear stability property. Drew and Passman (1999) argued that a well-posed viscous TFM is still practically ill-posed because the wave growth rate remains high and the model has exponential blow up. Indeed the TFM would be unacceptable if the surface waves kept on growing unboundedly. But linear stability analysis turns out to be insufficient because unstable surface waves in their very nature either break or peak, and both these phenomena are nonlinear. So the ultimate question is whether a TFM is Lyapunov stable, i.e., whether there is a nonlinear mechanism to bound wave growth. It turns out that viscosity is involved in a key nonlinear mechanism that makes the largest Lyapunov exponent of wavy stratified flow one order of magnitude smaller than the maximum linear growth rate, as shall be demonstrated in Chap. 4, and bounds the growth of the waves after a certain point.

2.4.2 Dispersion Relation for the SWT Instability ($F \neq 0$)

We have considered the dynamic KH instability in the previous section. We now consider the kinematic instability caused by the wall and interfacial friction forces, i.e., the SWT instability, following the analysis of Lopez de Bertodano et al. (2013). Kocamustafaogullari (1985) was the first to adopt a full TFM formulation for the case of thin falling liquid films with interfacial shear. His analysis, which gives very similar results to Anshus and Goren (1966) using the Orr–Sommerfeld equation, includes the velocity shape factor term for the liquid film in addition to the effects of evaporation and condensation, which are not considered in this book. Later the TFM analysis for cocurrent adiabatic two-phase flow in a duct was performed by Barnea and Taitel (1993) who labeled this instability the Viscous Kelvin–Helmholtz

instability. It is related to the kinematic waves described by Lighthill and Whitham (1955), also called void waves or continuity waves by Wallis (1969).

Before performing the stability analysis it is necessary to define a kinematic wave for the 1D FFM. To consider the mathematics that leads to a kinematic instability in the two-equation model we include the frictional and drag (i.e., viscous) forces, F , in the momentum equation and disregard viscosity and surface tension from Eqs. (2.37) and (2.38) to obtain the SWT equations, cf. Appendix B.5.1:

$$\frac{\partial \alpha}{\partial t} + u \frac{\partial \alpha}{\partial x} + \alpha \frac{\partial u}{\partial x} = 0, \quad (2.47)$$

$$\frac{\partial u}{\partial t} + u \frac{\partial u}{\partial x} - C \frac{\partial \alpha}{\partial x} = F, \quad (2.48)$$

where F is defined by Eq. (2.32). This results in the dispersion relation given by Eq. (B.56). We now apply the kinematic stability condition of Lighthill and Whitham (1955), i.e., $v_w = c$. For the specific case of the frictional forces of the TFM we will use $F = F(\alpha_1, u_1, u_2)$ instead of $F = F(\alpha_1, u_1)$ to derive the kinematic wave speed. Then applying the definition of the kinematic wave speed (Wallis 1969) introduced in Appendix B.5,

$$v_w = u + \alpha_1 \left(\frac{\partial u_1}{\partial \alpha_1} \right)_F \quad (2.49)$$

together with the fixed flux condition, it can be shown that

$$v_w = u - \alpha_1 \left[\frac{(1 - \alpha_1) \frac{\partial F}{\partial \alpha_1} + (u_2 - u_1) \frac{\partial F}{\partial u_2}}{(1 - \alpha_1) \frac{\partial F}{\partial u_1} - \alpha_1 \frac{\partial F}{\partial u_2}} \right]. \quad (2.50)$$

Combining Eqs. (2.49) and (2.50), an algebraic formulation for the kinematic wave speed may be obtained, which enables the kinematic instability condition, i.e., $c - v_w = 0$, to be mathematically defined. But first it is convenient to obtain the dynamic instability condition in terms of the two independent variables, α_1, u_1 . Starting with the kinematic condition, $F = 0$ with $g_x = 0$,

$$-(1 - \alpha_1) \frac{f_1}{2} u_1^2 + \alpha_1 \frac{f_2}{2} r_\rho u_2^2 + \frac{f_i}{2} r_\rho (u_2 - u_1)^2 = 0 \quad (2.51)$$

yields u_2 in terms of $\alpha = \alpha_1$ and $u = u_1$, that is:

$$u_2 = \frac{f_i r_\rho u + \sqrt{-r_\rho u^2 [f_2 f_i r_\rho \alpha - f_1 (f_i + f_2 \alpha)(1 - \alpha)]}}{r_\rho (f_i + f_2 \alpha)}. \quad (2.52)$$

It can be seen that the term containing f_2 in Eq. (2.51) becomes negligible in the limit $\alpha \rightarrow 0$, which corresponds to low values of j_1 . Neglecting the f_2 term greatly simplifies the analysis. The dynamic stability condition $C = 0$, with C defined by Eq. (2.35), results in the following critical liquid velocity for dynamic instability:

$$u_{\text{dyn}} = \pm \sqrt{\frac{f_i}{f_1} g_y H}. \quad (2.53)$$

The kinematic stability condition, $c = v_w$, reduces into a quadratic equation for u :

$$f_i g H \bar{f} - f_1 \left[\bar{f} + f_i \frac{9}{4} (1 - \alpha) \alpha \right] u^2 = 0, \quad (2.54)$$

where

$$\bar{f} = \left(\sqrt{f_1 (1 - \alpha)^3} + \sqrt{f_i r_p} \right)^2. \quad (2.55)$$

Finally, Eq. (2.54) may be solved to obtain the critical liquid velocity for the kinematic instability,

$$u_{\text{kin}} = u_{\text{dyn}} \sqrt{\frac{1}{1 + \frac{9}{4} \frac{f_i}{\bar{f}} \alpha (1 - \alpha)}}. \quad (2.56)$$

This simple analytic result leads to some straightforward insights for gas–liquid flows. First, $u_{\text{kin}} \leq u_{\text{dyn}}$ unconditionally. Second, $u_{\text{kin}} \rightarrow u_{\text{dyn}}$ when $\frac{f_i}{\bar{f}} \rightarrow 0$. For example, consider conditions $r_p = 0.001$, $f_1 = 0.005$, $f_i = 0.014$ (Cohen and Hanratty 1965), and $H = 50$ mm, shown in Fig. 2.6. These values are similar to the TFM analysis of Barnea and Taitel (1993) for stratified flow shown in Fig. 2.7, the difference in the results is due primarily to the different geometries (i.e., parallel plates vs. a pipe). Furthermore, Barnea and Taitel (1994) performed an analysis with the FFM Eqs. (2.47) and (2.48) but with a slightly different form of Eq. (2.35), i.e., $C = r_p \frac{u_2^2}{1 - \alpha_1} - (1 - r_p) g_y H$, for flow between parallel plates, where it is assumed that the gas velocity is much greater than the liquid velocity. For a round tube they got practically the same results as those in Fig. 2.7, which validates the use of the simplified FFM analysis given by Eqs. (2.47) and (2.48) instead of the TFM analysis.

Increasing the liquid viscosity by a large amount, from $\nu = 1 \times 10^{-6}$ m²/s to $\nu = 500 \times 10^{-6}$ m²/s, makes the kinematic and dynamic instabilities approach each other because $\frac{f_i}{\bar{f}} \rightarrow 0$, see Eq. (2.56). Thus, the difference of the two stability

Fig. 2.6 Stability map for stratified flow between horizontal parallel plates, reprinted from Lopez de Bertodano et al. (2013), with permission from Begell House

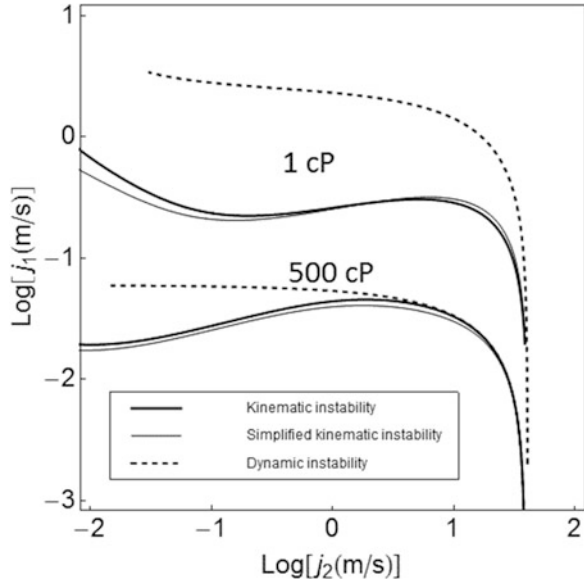
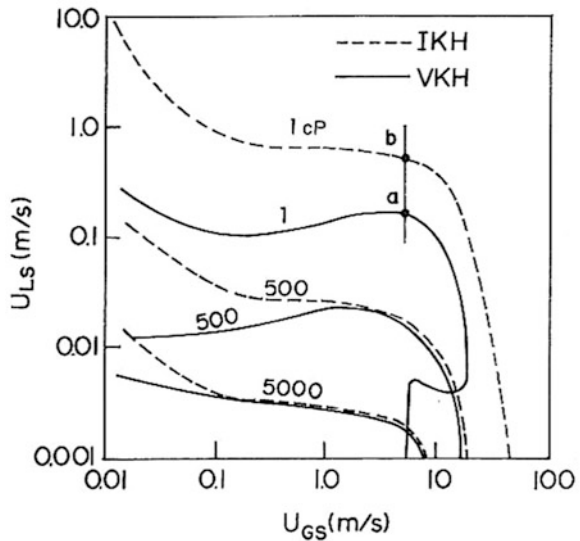


Fig. 2.7 Stability map for stratified flow in a horizontal pipe, reprinted from Barnea and Taitel (1993), with permission from Elsevier



boundaries is negligible for very viscous liquid flows, e.g., oil–gas flows vs. water–gas flows.

The stability result for the full Eq. (2.52), i.e., including f_2 , way also obtained and a quadratic equation for u was derived, leading to an analytic solution considerably more complicated than Eq. (2.56), which will not be presented here. However, the

results for $f_2 = 0.005$ are shown in Fig. 2.6 and they are very close to the simplified results with $f_2 = 0$.

Finally, it is desirable to demonstrate that the source term, F , may be neglected from the analysis when the flow becomes dynamically unstable, so that the dynamic stability analysis performed in Sect. 2.4.1 may be shown to stand on its own. The objective is to show that the kinematic instability becomes negligible once the KH condition is exceeded. This derivation follows the numerical results of Barnea and Taitel (1993) comparing the wave growth rates for the kinematic and dynamic instabilities for gas–liquid flows. It will be shown that the growth rate of the dynamic instability is at least one order of magnitude higher than the growth of the kinematic instability when these occur simultaneously, so the latter may be neglected.

The wave growth rate for the dynamic instability is given by Eq. (2.45),

$$\omega_{\text{dyn,max}} = \sqrt{\frac{\alpha\rho_1}{\sigma H} \left[\frac{\rho_2}{\rho_1} \frac{(u_2 - u_1)^2}{\alpha_2} - gH \right]^2} \sim \sqrt{\frac{\alpha\rho_1}{\sigma H} [g_y H]^2}. \quad (2.57)$$

The dispersion relation for the kinematic instability is given by Eq. (B.56),

$$\omega_{1,2} = uk + i\frac{F_u}{2} \pm \sqrt{\left(i\frac{F_u}{2} - ck\right)^2 + iF_u(c - v_w)k} \quad (2.58)$$

which has the following approximate Taylor expansion in terms of $(c - v_w)$:

$$\omega_1 \cong \frac{F_u}{2} \left[i \frac{\frac{4c(c - v_w)k^2}{F_u^2}}{\frac{8c^2k^2}{F_u^2} + 2} - \frac{2k(c - v_w)}{\frac{8c^2k^2}{F_u^2} + 2} \right] + (u + c)k. \quad (2.59)$$

The maximum wave growth rate then occurs in the limit as $k \rightarrow \infty$ which is given by

$$\omega_{\text{kin,max}} = i\frac{F_u}{4} \frac{(c - v_w)}{c} \sim -i\frac{F_u}{4}. \quad (2.60)$$

Taking the derivative of Eq. (2.32), and assuming $f_2 = 0$, leads to

$$F_u = -\left[\frac{1}{\alpha} \frac{f_1}{f_i r_\rho} + \left(\frac{1}{1 - \alpha} + \frac{1}{\alpha} \right) \sqrt{(1 - \alpha) \frac{f_1}{f_i r_\rho}} \right] f_i r_\rho \frac{u}{H} \sim -\frac{f_1 u}{H\alpha} \quad (2.61)$$

because the second term in the brackets becomes negligible as $r_p \rightarrow 0$. Combining Eqs. (2.60) and (2.61) then yields an approximate kinematic wave growth rate,

$$\omega_{\text{kin}, \max} \sim \frac{1}{4} \frac{f_1 u}{H \alpha}. \quad (2.62)$$

The ratio of the dynamic and kinematic wave growth rates then is

$$\frac{\omega_{\text{dyn}, \max}}{\omega_{\text{kin}, \max}} \sim 4\alpha \frac{g_y H^2}{f_1 u} \sqrt{\alpha \frac{\rho_1}{\sigma H}}. \quad (2.63)$$

For water flow with $\alpha = 0.2$, $\nu = 1 \times 10^{-6} \text{ m}^2/\text{s}$ and $j_1 = 0.1 \text{ m/s}$, this ratio is approximately 1400, and for oil with $\nu = 500 \times 10^{-6} \text{ m}^2/\text{s}$ the ratio is approximately 14. Therefore, for most cases of practical interest, once the dynamic instability is attained friction has little effect on the growth rate of the waves within the scope of the 1D TFM. This does not mean that friction terms are not important to the dynamics of the model, for they determine whether the flow reaches the KH instability, but they become irrelevant to the growth rate of the waves afterward and Eq. (2.42) suffices. Therefore, it is not necessary to develop a dispersion relation with the combined effects. In lieu of that, the dispersion relation is given by Eq. (2.58) when the liquid velocity reaches the kinematic instability velocity, i.e. Eq. (2.56), and by Eq. (2.42) when the liquid velocity is increased beyond the KH velocity, i.e. Eq. (2.52).

2.4.3 Sheltering Effect

While the FFM of the previous section is qualitatively correct for gas–liquid flows, it does not accurately predict the transition to wavy flow. To remedy the discrepancy Benjamin (1959) proposed a more complete picture of the interfacial force. There is a compression and expansion of the streamlines in the windward and leeward sides of the wave which leads to an increase and decrease in the interfacial shear respectively. Brauner and Maron (1993) incorporated this into the 1D TFM adding a void gradient in the interfacial shear:

$$\tau_i = \frac{f_i}{2} \rho_2 (u_2 - u_1)^2 + C_h \rho_2 (u_2 - u_1)^2 H \frac{\partial \alpha_1}{\partial x}, \quad (2.64)$$

where the first term on the RHS is the original steady drag component and the second term represents the sheltering effect with the coefficient

$$C_h = C_{h0} \left(\frac{Re_1}{Fr_1^2} \right)^m, \quad m = \min[1, 1.565 - 0.072 \ln(Re_1)]. \quad (2.65)$$

More recently, Kushnir et al. (2014) performed an Orr–Sommerfeld analysis that confirms this hypothesis, in particular for gas–liquid stratified flow. Furthermore, they obtained that the wall stresses also have a component that is in phase with the wave slope. This sheltering model is now incorporated into the FFM (Lopez de Bertodano et al. 2013).

The form of the coefficient, C_h , in Eq. (2.65) was determined by Brauner and Maron (1993) after an extensive comparison with experimental data. The leading coefficient, C_{h0} , was adjusted in the present model from 0.000245 up to 0.0004 to account for the difference in flow geometry, i.e., rectangular channel HAWAC data of Vallee (2010) vs. pipe flow data used by Brauner and Maron (1993).

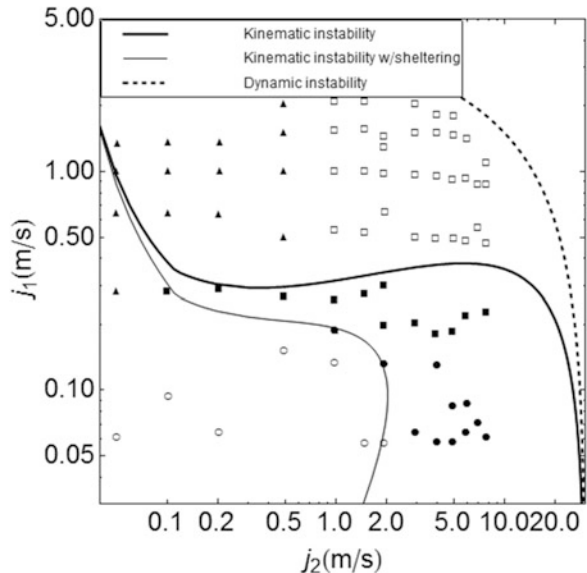
Equations (2.64) and (2.65) were added to the FFM and the linear stability analysis of the previous section was repeated. The modified KH criterion, cf. Eq. (2.36),

$$(u_2 - u_1)^2 = \frac{1}{r_\rho} \frac{gH}{\frac{1}{1-\alpha_1} + C_h \left(\frac{1}{\alpha_1} + \frac{1}{\alpha_2} \right)} \quad (2.66)$$

was derived from the characteristic analysis.

The sheltering force has a considerable destabilizing effect. The SWT stability criteria with and without the sheltering effect are compared to the HAWAC data of Vallee (2010) in Fig. 2.8, where $j_k = \alpha_k u_k$, $k = 1, 2$. The stable region is in the lower left corner, the flow is SWT stable below the solid lines and KH unstable above the dashed line. It can be observed that all the wavy-stratified flow data,

Fig. 2.8 Stability Map of the HAWAC experiment of Vallee et al. (2010). Symbols denote flow regimes: *open circle* stratified smooth, *filled circle* stratified wavy, *filled square* transition, *filled triangle* elongated bubble, *open square* slug, reprinted from Lopez de Bertodano et al. (2013), with permission from Begell House



which was previously in the stable region, is shifted to the unstable region. Therefore, including the effects of wave sheltering in the steady drag force marks a significant improvement to the prediction of unstable air–water stratified flow data.

2.5 Numerical Stability

2.5.1 *Obtaining a Well-Posed Numerical Model*

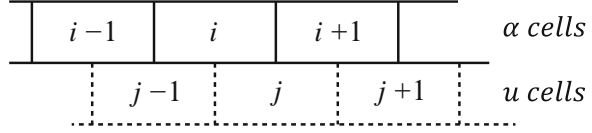
The ill-posed nature of an incomplete TFM has led to different approaches being used to obtain a well-posed numerical model. The first approach has been to seek added modeling detail to render the differential model well-posed. The general logic behind this approach is that since the physical problem and the Navier–Stokes equations are well-posed, something must have gone astray in the process of averaging the TFM to obtain a macroscopic description. Often the added differential model is artificial and its object is to hyperbolize the TFM. While this may not be physically correct it may be an acceptable compromise if supported by tuning with experimental data, at the cost of losing generality. An example will be given in Chap. 8.

The second approach has been to simply use numerical viscosity which damps the short wavelength components of the numerical solution. This approach parallels the methods which are used for modeling turbulent flow, in which the small-scale eddies responsible for viscous dissipation are not directly resolved, and damping at an intermediate wavelength is imposed through a viscosity correlation that acts as a filter providing dissipation and stability. In this case, the intermediate wavelength should be chosen short enough that the large-scale motion is not affected. The basic reason that this approach may be successful is the existence of the turbulent “energy cascade” in which it is not the short wavelength phenomena that govern the rate of energy dissipation, but rather it is governed by the rate at which energy is injected into the cascade by the long wavelength motion. Thus, it is only necessary to model the dissipation process at a sufficiently small scale so that the mean motion remains unaffected. While the incomplete TFM stability is not so simple, we may proceed with this idea for now and improve upon it later.

2.5.2 *First-Order Semi-Implicit Scheme (Inviscid)*

We choose a semi-implicit scheme for the FFM that is closest to is the one used in the TFM-TFIT code of Chap. 3. It is a combination of the explicit and implicit

Fig. 2.9 Staggered continuity cells and momentum junctions



schemes presented in Appendices B.4.1 and B.4.2, respectively. The finite difference equations are as follows:

$$\frac{\alpha_i^{n+1} - \alpha_i^n}{\Delta t} + \frac{u_R^{n+1} \hat{\alpha}_R^n - u_L^{n+1} \hat{\alpha}_L^n}{\Delta x} = 0, \quad (2.67)$$

$$\frac{u_j^{n+1} - u_j^n}{\Delta t} + u_j^n \frac{u_j^n - u_{j-1}^n}{\Delta x} - C \frac{\alpha_R^n - \alpha_L^n}{\Delta x} = 0. \quad (2.68)$$

Equation (2.68) is solved first so that the updated velocities can be used in Eq. (2.67). Due to the staggered grid, shown in Fig. 2.9, some “R” and “L” data are available but $\hat{\alpha}_R^n = \alpha_{i+1/2}^n$ does not exist and it is “donored,” i.e., for positive SWT wave speed $c = u + \sqrt{-C\alpha}$ and FOU, $\hat{\alpha}_R^n = \alpha_i^n$.

This scheme illustrates the effect that a staggered mesh has on consistency and stability. Equations (2.67) and (2.68) can be rearranged to show that staggering is equivalent to the introduction of higher order difference terms for finite mesh intervals; however, these terms do not always contribute a damping effect. We will use the terminology of “cell” to refer to the center of the control volume for mass, and “junction” to refer to the center of the momentum control volume at which the velocity is evaluated (i.e., the edges of the mass cells).

The stability property of a numerical scheme concerns the manner in which the numerical solution diverges away from the exact solution. In the case of linear systems it is possible to analytically establish the solution divergence and to develop necessary and sufficient conditions to ensure stability. In the more general case of nonlinear systems, it is necessary to linearize the equations in order to obtain analytical solutions for the differential and difference equations. Thus one cannot obtain, in general, neither necessary nor sufficient conditions to ensure a particular type of divergence between the “exact” and numerical solutions. Experience has shown that local stability in the von Neumann sense, Richtmeyer and Morton (1967), is necessary in most cases and in many, sufficient as well. The von Neumann criterion for stability, described in Appendix B.4, requires that the magnitude of the eigenvalues of the amplification matrix, \mathbf{G} , satisfies the inequality Eq. (B.30):

$$|\mathbf{G}|_{\max} \leq 1 + O(\Delta t), \quad (2.69)$$

where $|G|_{\max}$ is the maximum eigenvalue of G . The growth matrix G for the difference scheme is defined by the recursion relation

$$\underline{\phi}^{n+1} = G \underline{\phi}^n. \quad (2.70)$$

Equation (2.69) is called a stability condition, but in reality it is a requirement that the difference problem be well-posed, i.e., the wave growth rate remains bounded in the limit as the mesh is refined to zero. This is consistent with the well-posedness criterion that the growth rate of the differential model must remain finite at all wavelengths,

$$|G|_{\max}^N \equiv e^{-I\omega_1^\Delta t} \cong \prod_{n=0}^N (1 \pm |\omega_1^\Delta| \Delta t_n), \quad (2.71)$$

where the sign depends on whether the *differential problem* is stable or unstable. The eigenvalues of G are functions of the Fourier component wavelength and, for a given node network, the spatial wavelengths of interest range from $2\Delta x$ to infinity. A difference scheme is unconditionally stable if Eq. (2.69) is satisfied for all values of the time step, Δt . For hyperbolic systems without source terms the stability criterion, Eq. (2.69), can be reduced to $|G|_{\max} \leq 1 + O(\Delta t)^m$, where m is the order of the truncation error and is at least two for any practical numerical scheme. Only when source terms are present, e.g., the kinematic instability discussed in Sect. 2.4.2, it is necessary to reduce the stability requirement to Eq. (2.69). As long as source terms are approximated consistently in the difference scheme, they do not affect stability.

To clarify the relationship between the numerical scheme and the differential equation system, consider Fig. 2.4. Here the growth coefficients of the differential equation, $-I\omega_1^\Delta > 0$, for the ill-posed ($\epsilon = \nu = 0$) and well-posed ($\epsilon, \nu > 0$) cases, are plotted at a fixed time for the range of wavelengths of interest. For all systems the long wavelengths have a growth approaching the one due to the K–H instability alone. However, for the ill-posed case, additional unbounded growth occurs at short wavelengths, whereas for the parabolic case the growth is mitigated due to the $e^{-\frac{1}{2}(\epsilon+\nu)k^2 t}$ term from the dispersion relation, Eq. (2.42). Therefore, if the differential equations are hyperbolic or parabolic the growth rate is bounded and the problem is well-posed. Any numerical solution scheme that satisfies Eq. (2.69) will then result in a well-posed numerical problem.

In turn, if the differential equations are ill-posed it is not clear what requirement should be placed on a numerical solution scheme. Such a case may occur when some real physical process has been omitted or modeled inappropriately by filtering relevant mechanisms, e.g., an incomplete TFM. If one is sure that the long wavelength behavior described by the ill-posed system is basically correct and the short wavelength behavior is not crucial, then the system can be modified arbitrarily in the short wavelength range to obtain bounded growth. A numerical scheme for the modified differential system can be required to satisfy Eq. (2.69) and thus result in a well-posed numerical problem. In such case the differential equations could be modified by the inclusion of derivative terms which stabilize the short wavelengths.

The inclusion of physical or artificial stabilization at short wavelength has two effects. The first, mentioned earlier, is to give bounded growth rates at short wavelengths. The second effect occurs in nonlinear equations, and is not revealed by the linear analysis; whereas, the nonlinear terms can cause dispersion in which a solution component, having a growth rate greater than unity, disperses into longer and shorter wavelength components. Eventually, energy is cascaded to a short wavelength where the growth rate is less than unity and is dissipated. Thus, energy is removed from the unstable solution components. By this process the dissipation at short wavelength can limit the growth at longer wavelengths. For example, as shown in Appendix B.3.1, the one-dimensional Burgers' waves dissipate energy at the shock-like fronts.

The von Neumann analysis introduced in Appendix B.4.1 for the one-way wave equation is now extended to the FFM. The growth matrix for a general two-level difference scheme is defined by Eq. (2.70). The explicit form of the amplification matrix for a particular differencing scheme can be obtained by expressing the spatial variation of ϕ about the point ϕ_j^n in terms of a typical Fourier component, i.e.,

$$\phi_l^n = \phi_j^n e^{Ik(l-j)\Delta x}, \quad (2.72)$$

where k is the corresponding wavenumber. Using Eq. (2.72), Eqs. (2.67) and (2.68) may be written as:

$$\underline{M}\underline{\phi}^{n+1} = \underline{N}\underline{\phi}^n. \quad (2.73)$$

The corresponding FOU growth matrix then becomes $\underline{G} = \underline{M}^{-1}\underline{N}$ where

$$\underline{M} = \begin{bmatrix} e^{\frac{Ik\Delta x}{2}} & \frac{\alpha\Delta t(e^{Ik\Delta x} - 1)}{\Delta x} \\ 0 & 1 \end{bmatrix}, \quad (2.74)$$

$$\underline{N} = \begin{bmatrix} e^{\frac{Ik\Delta x}{2}} - \frac{2Iu\Delta t \sin\left[\frac{k\Delta x}{2}\right]}{\Delta x} & 0 \\ \frac{2Ic\Delta t \sin\left[\frac{k\Delta x}{2}\right]}{\Delta x} & 1 - \frac{u\Delta t(1 - e^{-Ik\Delta x})}{\Delta x} \end{bmatrix} \quad (2.75)$$

and the eigenvalues are as follows:

$$|\mathbf{G}| = 1 - \frac{\Delta t(1 - e^{-Ik\Delta x})}{2\Delta x^2} \left[C\alpha\Delta t(e^{Ik\Delta x} - 1) + 2u\Delta x \right. \\ \left. \pm \sqrt{C\alpha} \sqrt{C\alpha\Delta t^2(e^{Ik\Delta x} - 1)^2 - 4\Delta x[u\Delta t + (\Delta x - u\Delta t)e^{Ik\Delta x}]} \right]. \quad (2.76)$$

The stability of the numerical scheme is compared to the stability of the differential model by evaluating the eigenvalues of the growth matrix for a range of wavelengths. The difference scheme growth rate is defined by Eq. (B.32):

$$\omega_1^\Delta = -I \frac{\ln|\mathbf{G}|_{\max}}{\Delta t}, \quad (2.77)$$

i.e., the finite difference growth rate is compared to the growth rate of the dispersion relation of the partial differential equations (2.42). A numerical imaginary wave speed, corresponding to the wave growth speed, may also be considered:

$$c_1^\Delta = -I \frac{\ln|\mathbf{G}|_{\max}}{k\Delta t}. \quad (2.78)$$

Stable model ($C < 0$)

The Courant–Friedrichs–Lewy (CFL) criterion for SWT $Co \equiv (u + \sqrt{-C\alpha}) \Delta t / \Delta x = 1$ determines the stability limit of the FOU numerical method. The behavior of the semi-implicit scheme for the stable well-posed model, with $Co = 0.5$, 1 , $C = -1$, $\alpha = 0.5$, and $u = 1.0$, is shown in Fig. 2.9. The growth rate is plotted in the imaginary plane for $0 < k\Delta x < 2\pi$. There are two eigenvalues and the most important feature of this plot is that $|\mathbf{G}| \leq 1$ when $Co = 0.5$ for both of them, whereas $|\mathbf{G}| = 1$ for $Co = 1.0$, i.e., the wave amplitude is constant. This is the well-known stability condition for stable numerical schemes. Figures 2.10 and 2.11 show the Von Neumann analysis results in the growth vs. wavelength plane. When $Co = 0.5$ the growth rates are less than zero for short wavelengths as expected for a scheme with numerical viscosity, but the growth rates become greater than zero when $Co = 1.5$, so the numerical scheme is now unstable, i.e., the CFL condition is exceeded. The next question is what happens when the equations are unstable so that growth occurs in the differential model to begin with?

Unstable model ($C > 0$)

The stability characteristics of the numerical scheme are compared by plotting the growth rates of the finite-difference system and the ill-posed differential system in Fig. 2.12. The character of the difference scheme is contrasted to the differential system by presenting the relative amplification factors to illustrate applicability of the upwind numerical scheme to ill-posed problems. Figure 2.11 shows the results for $\Delta x = 0.005$, 0.01 and 0.02 m and the dispersion relation result for the Euler FFM with $Co = 0.5$.

Fig. 2.10 Growth rate map for stable model

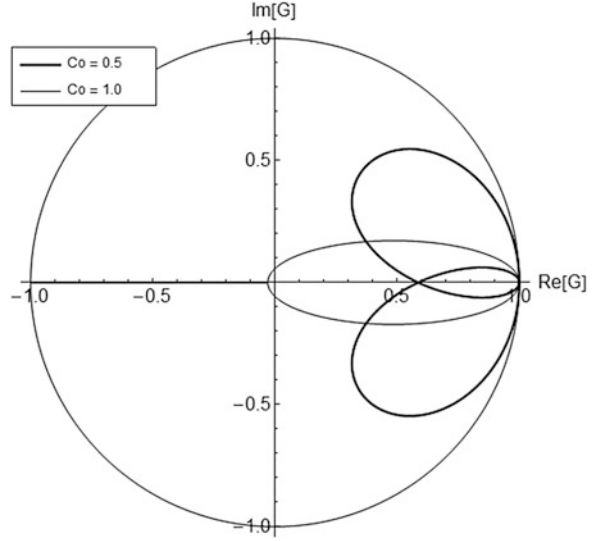
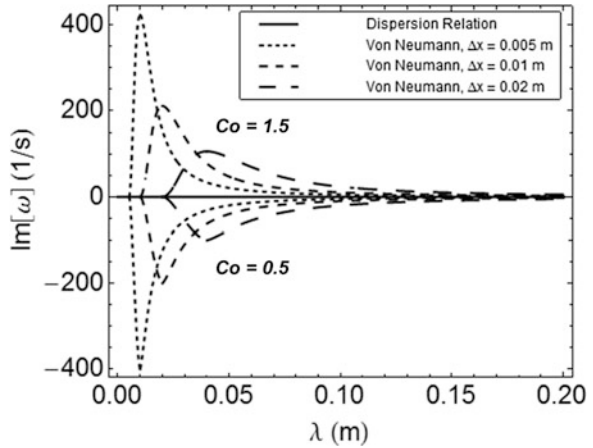


Fig. 2.11 FOU stability, stable model



The differential model growth rate is an exponential function and becomes unbounded as the mesh is shrunk to zero ($\Delta x \rightarrow 0$), i.e., ill-posed. In order to obtain a well-posed finite-difference problem for finite Δx , the difference scheme should attenuate the exponential growth of the differential system and result in a growth rate less than 0 at the smallest wavelength of interest (i.e., $2 \Delta x$). The semi-implicit scheme with a staggered mesh shows a continual decrease in growth rate for wavelengths $\lambda < 5 \Delta x$. This is a convenient engineering solution to an ill-posed problem; however, the cutoff wavelength decreases with mesh size and then the numerical solution does not converge.

Fig. 2.12 FOU stability, unstable model, $Co = 0.5$

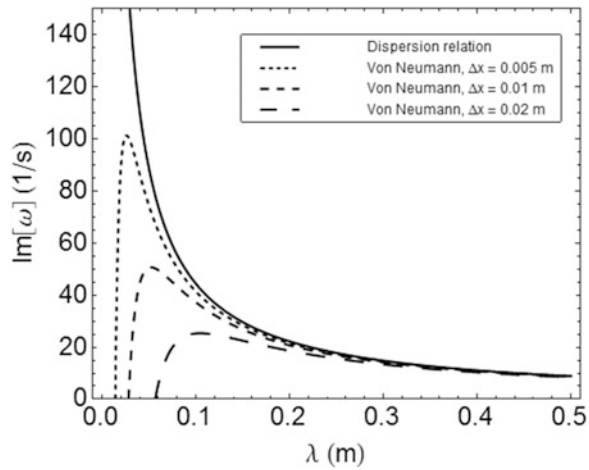
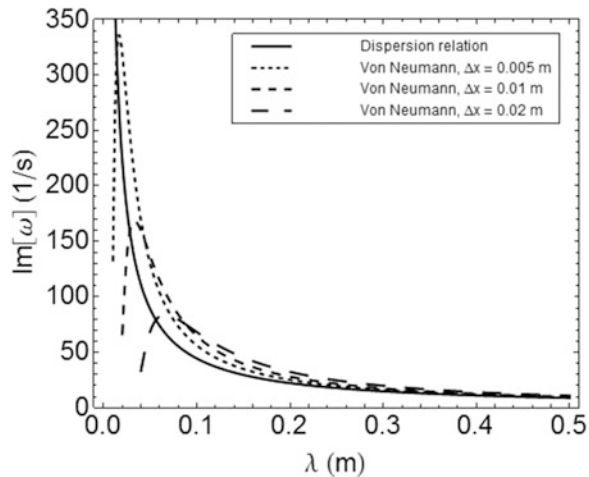


Fig. 2.13 FOU stability, unstable model, $Co = 1.5$



As was shown in the previous section, the numerical method becomes unstable for a Courant number greater than one. For example Fig. 2.13 shows the growth rates with $Co = 1.5$ where the numerical results are *more unstable* than the differential model.

Numerical viscosity is an effective expedient to solve the TFM simply because it damps the short wavelengths of the solution when the TFM becomes KH unstable and ill-posed, as described in section 2.4. However, the numerical model does not converge.

A low pass filter consisting of artificial viscosity terms in the continuity and momentum equations, makes the TFM well-posed and is a better alternative to numerical viscosity, because the numerical model then converges and the cutoff wavelength may be prescribed precisely. The next section illustrates the artificial viscosity solution. The derivation of a low pass filter is presented in Chap. 8.

2.5.3 First-Order Semi-Implicit Scheme (with Viscous Terms)

It was argued in the previous section that the FFM becomes well-posed if a low pass filter, consisting of an artificial viscous term, is added to the two equations. We now write a semi-implicit finite difference model with artificial implicit center-difference viscous terms, i.e., $\varepsilon = \nu$, for a FFM with an arbitrary filter, i.e., $\varepsilon = \nu$:

$$\frac{\alpha_i^{n+1} - \alpha_i^n}{\Delta t} + \frac{u_R^{n+1} \hat{\alpha}_R^n - u_L^{n+1} \hat{\alpha}_L^n}{\Delta x} = \nu \frac{\alpha_{i+1}^{n+1} - 2\alpha_i^{n+1} + \alpha_{i-1}^{n+1}}{\Delta x^2}, \quad (2.79)$$

$$\frac{u_j^{n+1} - u_j^n}{\Delta t} + u_j^n \frac{u_j^n - u_{j-1}^n}{\Delta x} - C \frac{\alpha_R^n - \alpha_L^n}{\Delta x} = \nu \frac{u_{j+1}^{n+1} - 2u_j^{n+1} + u_{j-1}^{n+1}}{\Delta x^2}. \quad (2.80)$$

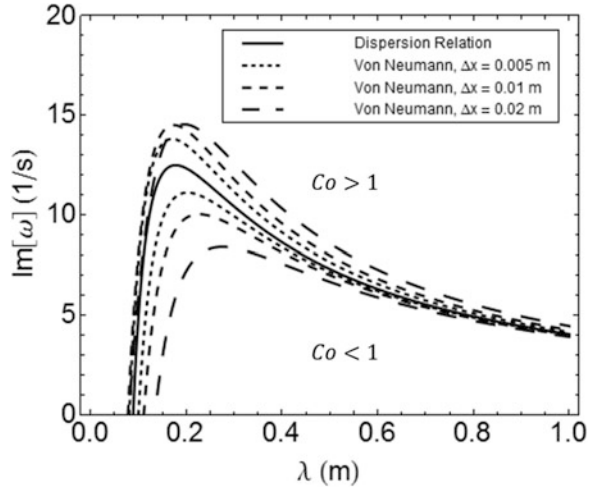
This numerical model is still Courant number limited. The von Neumann analysis is performed following the procedure outlined in the previous section. The matrices now are

$$N = \begin{bmatrix} e^{\frac{Ik\Delta x}{2}} - \frac{2I\nu \Delta t (e^{Ik\Delta x} - 1) \sin \left[\frac{k\Delta x}{2} \right]}{\Delta x^2} & \frac{\alpha \Delta t (e^{Ik\Delta x} - 1)}{\Delta x} \\ 0 & 1 - \frac{2\nu \Delta t (\cos [k\Delta x] - 1)}{\Delta x^2} \end{bmatrix}, \quad (2.81)$$

$$M = \begin{bmatrix} e^{\frac{Ik\Delta x}{2}} - \frac{2I\Delta t u \sin \left[\frac{k\Delta x}{2} \right]}{\Delta x} & 0 \\ \frac{2Ic\Delta t \sin \left[\frac{k\Delta x}{2} \right]}{\Delta x} & 1 - \frac{u\Delta t (1 - e^{-Ik\Delta x})}{\Delta x} \end{bmatrix}. \quad (2.82)$$

The equation for the eigenvalues of the growth matrix is more complicated than Eq. (2.76) and is not shown. Figure 2.14 shows the result of the growth rate of the von Neumann analysis compared with the dispersion relation using the same value for the viscosity (i.e., $\nu = 0.01 \text{ m}^2/\text{s}$ and $Co = 0.5$). The result is that the numerical model is also well-posed and the exponential growth of the numerical model is always smaller than that of the differential model, and both approach each other as the mesh resolution increases. It is important to note that the cutoff wavelength decreases with the mesh size, but converges, unlike the inviscid case. For the case with $Co = 1.5$, also shown in Fig. 2.14, the numerical model is consistent but the numerical solutions are more unstable than the exact one as the mesh is refined.

Fig. 2.14 FOU stability, effect of implicit diffusion ($Co = 0.5, 1.5$)



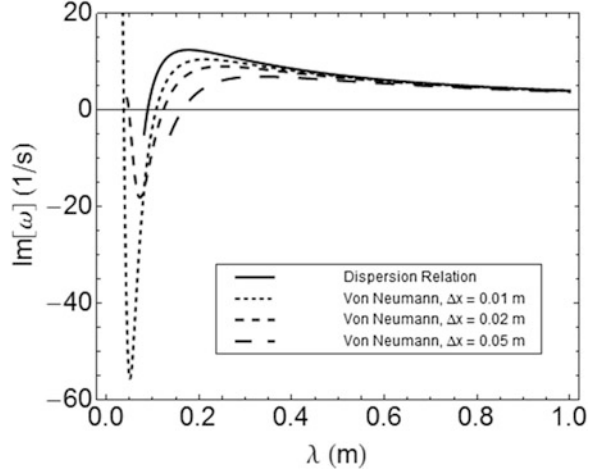
The case with explicit viscous terms is of interest because the stability of the model depends on the diffusion number, $R = \frac{\Delta t}{\Delta x^2}$, in addition to the Courant number. The von Neumann analysis matrices of the scheme with explicit viscous terms are as follows:

$$N = \begin{bmatrix} e^{\frac{Ik\Delta x}{2}} & \frac{\alpha\Delta t(e^{Ik\Delta x} - 1)}{\Delta x} \\ 0 & 1 \end{bmatrix}, \quad (2.83)$$

$$M = \begin{bmatrix} e^{\frac{u\Delta x}{2}} - \frac{2I\Delta t u \sin\left[\frac{k\Delta x}{2}\right]}{\Delta x} + \frac{2I\nu\Delta t(e^{Ik\Delta x} - 1)\sin\left[\frac{k\Delta x}{2}\right]}{\Delta x^2} & 0 \\ \frac{2Ic\Delta t \sin\left[\frac{k\Delta x}{2}\right]}{\Delta x} & 1 - \frac{u\Delta t(1 - e^{-Ik\Delta x})}{\Delta x} + \frac{2\nu\Delta t(\cos[k\Delta x] - 1)}{\Delta x^2} \end{bmatrix}. \quad (2.84)$$

Figure 2.15 shows the results of the von Neumann analysis for $Co = 0.5$ and $\Delta x = 0.01 - 0.05$ m. The corresponding values of the diffusion number are $R = 0.1 - 0.5$. The graphic shows that the numerical model is ill-posed at $\Delta x = 0.01$ m, a result that is well known from the numerical analysis of the one-way wave convection–diffusion equation (Strang 2007). This then poses a more severe constraint on the time step than the Courant criterion as the mesh is refined. Furthermore, there is another constraint with the dispersion of the solution that is determined by the Peclet number which is also addressed by Strang (2007). Because of these difficulties the diffusion terms are usually treated implicitly.

Fig. 2.15 FOU stability, effect of explicit diffusion ($Co = 0.5, R = 0.1 - 0.5$)



2.5.4 First-Order Fully Implicit Scheme (with Viscous Terms)

A fully implicit scheme has the advantage that it is not Courant number limited. The first-order implicit scheme for the one-way wave equation presented in Appendix B.4.2 is now applied to the FFM:

$$\frac{\alpha_i^{n+1} - \alpha_i^n}{\Delta t} + \frac{u_R^{n+1} \hat{\alpha}_R^{n+1} - u_L^{n+1} \hat{\alpha}_L^{n+1}}{\Delta x} = \nu \frac{\alpha_{i+1}^{n+1} - 2\alpha_i^{n+1} + \alpha_{i-1}^{n+1}}{\Delta x^2}, \quad (2.85)$$

$$\frac{u_j^{n+1} - u_j^n}{\Delta t} + u_j^{n+1} \frac{u_j^{n+1} - u_{j-1}^{n+1}}{\Delta x} - C \frac{\alpha_R^{n+1} - \alpha_L^{n+1}}{\Delta x} = \nu \frac{u_{j+1}^{n+1} - 2u_j^{n+1} + u_{j-1}^{n+1}}{\Delta x^2}. \quad (2.86)$$

The von Neumann matrices for this scheme are as follows:

$$N = \begin{bmatrix} e^{\frac{ik\Delta x}{2}} + \frac{2lu\Delta t \sin\left[\frac{k\Delta x}{2}\right]}{\Delta x} - \frac{2lv\Delta t(-1 + e^{ik\Delta x}) \sin\left[\frac{k\Delta x}{2}\right]}{\Delta x^2} & \frac{\alpha\Delta t(-1 + e^{ik\Delta x})}{\Delta x} \\ -\frac{2lC\Delta t \sin\left[\frac{k\Delta x}{2}\right]}{\Delta x} & 1 + \frac{u\Delta t(1 - e^{-ik\Delta x})}{\Delta x} - \frac{2\nu\Delta t(-1 + \cos[k\Delta x])}{\Delta x^2} \end{bmatrix}, \quad (2.87)$$

$$M = \begin{bmatrix} e^{\frac{ik\Delta x}{2}} & 0 \\ 0 & 1 \end{bmatrix}. \quad (2.88)$$

Fig. 2.16 FOU implicit scheme stability, unstable model, $Co = 5$

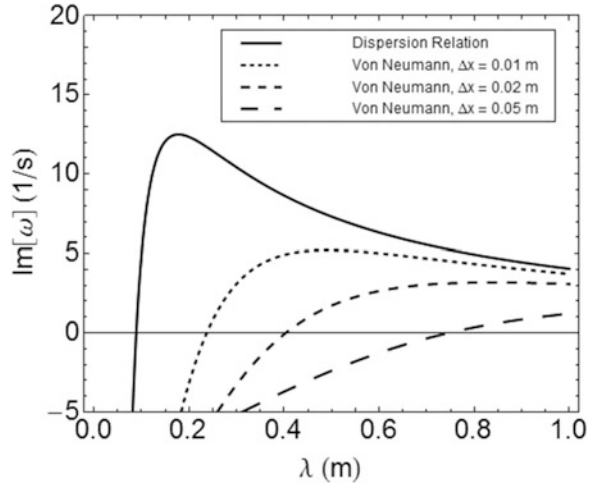
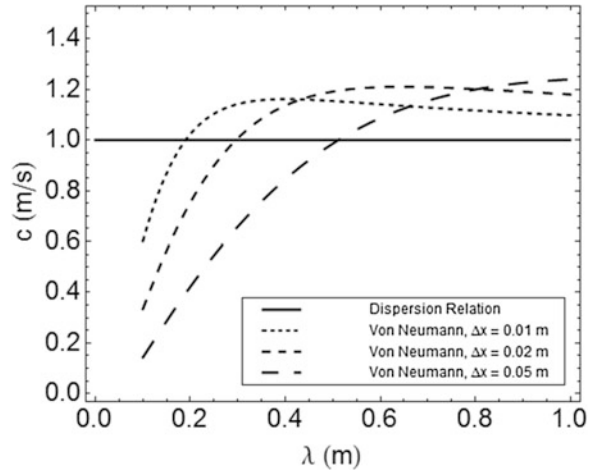


Fig. 2.17 FOU implicit scheme stability, unstable model, $Co = 5$



The main advantage of the implicit scheme is that long time steps may be used. To illustrate this point we consider a time step that is one order of magnitude longer, i.e., $Co = 5$ for the unstable case, i.e., $C = 1$. Figure 2.16 shows that the growth rate is significantly damped compared to the semi-implicit scheme, i.e., there is excessive numerical viscosity. Furthermore, Fig. 2.17 shows that there is excessive dispersion too, similar to the results in Appendix. B.4.2. Clearly long time steps deteriorate the accuracy of the wave propagation predictions and should be used with care. Such long time steps are only appropriate when material wave propagation phenomena are not relevant.

2.5.5 Second-Order Semi-Implicit Scheme

Appendix B.4.3 presented the well-known Lax–Wendroff second-order numerical scheme applied to the one-way wave equation. For practical reasons a different second-order numerical scheme is now proposed for the FFM, where the basic underlying structure, utilizing a staggered grid shown in Fig. 2.9, is maintained. This scheme shares similar wave propagation characteristics with the Lax–Wendroff scheme.

Equations (2.37) and (2.38) are arranged into the form

$$\frac{\partial}{\partial t} \phi = f_{\phi}(\alpha^{n\pm k}, u^{n\pm k}, r^{n\pm k}), \quad (2.89)$$

where the right-hand side functions, f_{ϕ} , are assumed to be known at each time level $n \pm k$ through a finite-difference scheme, and the time is advanced by treating the PDE as $2N$ ordinary differential equations (ODEs).

The finite-difference functions are given by

$$f_{\alpha,i} = -\bar{u} \frac{\hat{\alpha}_R - \hat{\alpha}_L}{\Delta x} - \alpha_i \frac{u_R - u_L}{\Delta x} + \varepsilon \frac{\alpha_{i+1} - 2\alpha_i + \alpha_{i-1}}{\Delta x^2} + S_{\alpha,i} \quad (2.90)$$

for the α equation at the i location and

$$f_{u,j} = -u_j \frac{\hat{u}_R - \hat{u}_L}{\Delta x} + C \frac{\alpha_R - \alpha_L}{\Delta x} + v \frac{u_{j+1} - 2u_j + u_{j-1}}{\Delta x^2} + S_{u,j} \quad (2.91)$$

for the u equation at the j location. The overbar indicates a cell averaged (mean) value. Variables with a hat do not exist at the specified location. The additional subscripts refer to the values to the “right” and “left” of the reference location. For example, in Eq. (2.90) the faces j and $j+1$ surround the reference i position, likewise for Eq. (2.91) the cell centers $i-1$ and i surround the reference j position. When the variables required at the right and left are available, they are used directly, e.g., u exists at j and $j+1$ in Eq. (2.90). When the variables do not exist at the right and left locations as indicated by the hat, they are donored or extrapolated using the values at the neighboring locations. A flux limiter is used for the extrapolation and discussed later. The diffusion terms are discretized with a standard second-order center difference scheme. For those simulations where periodic boundary conditions are applied three “ghost” cells are placed at the beginning and end of the domain that mirror the conditions at the opposite end.

For the extrapolated variables there are many options. Two obvious choices are first-order upwinding (FOU) and second-order center differencing. For the 1D FFM, the previous sections illustrated upwinding with edge values simply donored from adjacent cells in the direction of the SWT wave. The problem is that applying the FOU method to the convection variables adds a significant amount of numerical diffusion and lowers the accuracy of the entire scheme. On the other hand, viewing

the FFM equations as simply two PDEs, leaving physics considerations aside, one might opt for a center difference scheme. However, this would leave the overall finite difference scheme with all linear second-order difference stencils, leading to spurious numerical oscillations, which are undesirable for the present application where the underlying governing equations are already known to be unstable.

In order to combine increased accuracy and enhanced stability, a nonlinear flux limiter is used for the extrapolated variables (Drikakis and Rider 2005; Tannehill et al. 1997). This implies some physical interpretation in determining the direction of the “wind” or flow, here given by the sign of $c = u + \sqrt{-C\alpha}$. The general-piecewise limiter (GPL) of Waterson and Deconinck (2007) is used here because it is relatively simple and can easily be tuned to produce a variety of popular schemes.

The structure of the flux limiter for the right face value of the α variable in Eq. (2.90) is,

$$\hat{\alpha}_R = \alpha_i + \frac{\Delta x_i}{2} \Psi(r) \left(\frac{\partial \alpha}{\partial x} \right)_{UD}, \quad (2.92)$$

where r is the gradient ratio defined by,

$$r = \frac{\left(\frac{\partial \alpha}{\partial x} \right)_{CD}}{\left(\frac{\partial \alpha}{\partial x} \right)_{UD}}. \quad (2.93)$$

The subscripts CD and UD indicate the center and upwind differences for the location i . In the present work, a uniform mesh will always be applied so that Eq. (2.93) simplifies to

$$r = \frac{\alpha_{i+1} - \alpha_i}{\alpha_i - \alpha_{i-1}} \quad (2.94)$$

for positive flow, i.e., $c > 0$. The function $\Psi(r)$ is the flux limiter and the GPL scheme is given by

$$\Psi(r) = \max \left[0, \min \left\{ (2+a)r, \frac{1}{2}(1+k)r + \frac{1}{2}(1-k)r, M \right\} \right], \quad (2.95)$$

where a , k , and M are control parameters. The left values as well as the extrapolated variables of Eq. (2.91) are found in the same manner with the neighboring cell locations shifted appropriately.

The GPL limiter of Eq. (2.95) can be tuned to give several classical flux limiters, e.g., the Minmod scheme of Roe (1986) by setting $a = k = -1$ and $M = 1$ and the MUSCL scheme of van Leer (1979) by setting $a = k = 0$ and $M = 2$. In this work, the GPL scheme will be set to $a = 0$, $k = 1/2$, and $M = 4$, which results in the converted normalized variable SMART scheme of Gaskell and Lau (1988). The SMART scheme performed better for discontinuous solution data and was also

slightly higher than second-order accurate for smooth data. The SMART scheme has been selected since it is known in advance that the TFM equations produce solutions with shock-like structures, i.e., small regions of space where the solution changes rapidly. It should be pointed out that unlike Minmod and MUSCL, the limiter form of SMART is not exactly total variation diminishing (TVD). However, it is nonoscillatory in its original normalized variable form which has a rough equivalence to TVD (Drikakis and Rider 2005). The GPL can also be tuned to a few other schemes of less practical interest outlined by Waterson and Deconinck (2007). Additionally, by setting the limiter to the constants $\Psi(r) = 0$ or $\Psi(r) = 1$, the FOU and center difference schemes are recovered, respectively.

For the time advancement a Runge–Kutta method is selected. Rather than the standard fourth-order method that is often used, a strong stability preserving (SSP) third-order method is used in keeping with the theme of increased numerical stability. Essentially SSP schemes are the temporal equivalent to TVD spatial discretizations. The optimal third order, three stage (3-3) SSP Runge–Kutta method of Gottlieb and Shu (1998) is used to approximate Eq. (2.89), which is defined by

$$\begin{aligned}\phi^{(1)} &= \phi^n + \Delta t \cdot f_\phi(\alpha^n, u^n, t^n) \\ \phi^{(2)} &= \frac{1}{4}\phi^{(1)} + \frac{3}{4}\phi^n + \frac{1}{4}\Delta t \cdot f_\phi(\alpha^{(1)}, u^{(1)}, t^{n+1}) \quad , \\ \phi^{(n+1)} &= \frac{2}{3}\phi^{(2)} + \frac{1}{3}\phi^n + \frac{2}{3}\Delta t \cdot f_\phi(\alpha^{(2)}, u^{(2)}, t^{n+\frac{1}{2}})\end{aligned}\tag{2.96}$$

where Δt is the time step size between levels n and $n + 1$ and the difference functions are given in Eqs. (2.90) and (2.91).

This method is the most widely used SSP Runge–Kutta scheme since it is relatively inexpensive computationally and has a CFL criterion of unity. Combining the CFL condition with the restriction due to the explicit treatment of the diffusion terms, the resulting heuristic numerical stability constraint is

$$\Delta t \leq \min \left[\frac{\Delta x^2}{2\nu}, \frac{2\nu}{u_\infty^2} \right]\tag{2.97}$$

assuming $\varepsilon = \nu$ and $u_\infty = \max |u_j|$ in the domain.

In the end, the global method is a mix of second-order centered differences, fractional-order flux limited differences, and a third-order time marching scheme. The total accuracy of the combined scheme is as yet unknown, although one might expect it to fall somewhere between second- and third-order accuracy, the bounding upper and lower limits of the individual components. To answer this question and to determine if the resulting code has implemented these algorithms correctly, Sect. 2.6.4 will look at the problem of code verification by the method of manufactured solutions.

Section B.4.4 presented a second-order implicit scheme for the one-way wave equation. The major shortcoming is the significant increase in the dispersion of material waves, so the approach is not amenable to the simulation of material waves and is not pursued further since the purpose of higher-order accuracy in this book is precisely that.

2.6 Verification

2.6.1 Kreiss–Yström Equations

The numerical method described in the previous section was implemented using the Fortran programming language. As with any newly developed code, verification exercises should be performed. In general, verification is divided into two components: code verification and solution (or calculation) verification (Roache 1998, 2002). Code verification is the process of determining if the numerical algorithms were implemented correctly (Oberkampf and Roy 2010; Oberkampf et al. 2004) while solution verification deals with quantifying the numerical error of a given solution.

The present work focuses on the Kreiss and Yström (2002) system of partial differential equations (PDEs), which is remarkably similar to the FFM, given by

$$\frac{\partial \alpha}{\partial t} + u \frac{\partial \alpha}{\partial x} + \left[1 + \frac{\alpha}{2}\right] \frac{\partial u}{\partial x} = \varepsilon \frac{\partial^2 \alpha}{\partial x^2} - 2\alpha, \quad (2.98)$$

$$\frac{\partial u}{\partial t} + u \frac{\partial u}{\partial x} = C \frac{\partial \alpha}{\partial x} + \nu \frac{\partial^2 u}{\partial x^2} \quad (2.99)$$

and hereafter referred to as the KY equations. There are a few slight differences between the way we employ Eqs. (2.98) and (2.99) compared to the authors. First, the parameter C was unity in the original model. The adjustable coefficient C is used here as a means to vary the “degree of instability”, because it represents the KH criterion in Eqs. (2.37) and (2.38). Second, the viscosities have been given different symbols although the same value will be used for both.

Among the obvious differences in Eq. (2.98) and the FFM Eq. (2.37), the viscous term is significant because it acts like artificial viscosity in the TFM. Furthermore, there is another significant difference, the constraint $0 \leq \alpha \leq 1$ is not present. Nevertheless, the dynamic similarity of the KY equations and the FFM will be demonstrated in the next two sections and the nonlinear analysis of the KY equations in Ch. 4 is the preliminary step to approach the nonlinear behavior of the more complicated FFM, which is addressed afterward.

2.6.2 Characteristic Analysis

The FFM and the present Kreiss and Yström (2002) system are related in several significant ways. Both models are conditionally ill-posed as an initial and boundary value problem (IBVP) without higher order stabilization, i.e., the first-order systems (may) possess complex characteristics. Both models are predicted to be linearly unstable. The magnitude of the growth rates are linearly proportional to

the wavenumber without stabilization and quadratically damped at high wavenumbers with higher order stabilization. Both models have similar dynamics, i.e., they produce similar waveforms. However, the mathematical model of Kreiss and Yström (2002) is simpler in several desirable ways. It does not have a complicated flow-regime map of closure laws for different flow conditions—some of which affect the differential form of the governing equations. The dynamics of the problem are not bounded by physical constraints, e.g., channel height. It does not require special numerical techniques. Finally, and possibly most importantly, the “degree of instability” can be directly controlled by specifying the constant value of C in Eq. (2.86). In turn, in the 1D TFM of Eqs. (2.37) and (2.38) the coefficient is not constant but instead it is determined by the local flow conditions so that the linear stability of the model changes throughout the solution, and may even change from nonhyperbolic to hyperbolic depending on the flow conditions. Therefore, the simplified form and added controllability of the two KY equations make them an ideal first step for the nonlinear studies of Chap. 4.

The KY Eqs. (2.98) and (2.99) can be written in vector form as

$$\mathbf{A} \frac{\partial}{\partial t} \underline{\phi} + \mathbf{B} \frac{\partial}{\partial x} \underline{\phi} + \mathbf{D} \frac{\partial^2}{\partial x^2} \underline{\phi} = \underline{F}, \quad (2.100)$$

where the dependent variable vector is $\underline{\phi} = [\alpha, u]^T$, the source vector is $\underline{F} = [-2\alpha, 0]^T$, and the coefficient matrices are defined by

$$\mathbf{A} = \mathbf{I}, \quad \mathbf{B} = \begin{bmatrix} u & 1 + \frac{\alpha}{2} \\ -C & u \end{bmatrix}, \quad \mathbf{D} = \begin{bmatrix} -\varepsilon & 0 \\ 0 & -\nu \end{bmatrix}. \quad (2.101)$$

The eigenvalues of Eq. (2.99) are given by,

$$c = u \pm i \sqrt{C \left(1 + \frac{\alpha}{2} \right)}. \quad (2.102)$$

In the absence of diffusion, i.e., $\varepsilon = \nu = 0$, these eigenvalues define the characteristics of the system. Equation (2.102) shows that for $C > 0$ (and $\alpha > -2$) the characteristics are complex conjugates. Therefore, the system is ill-posed as an initial-boundary value problem. Even when the diffusion matrix is included, the complex characteristics are the central cause of the linear growth discussed later. On the other hand, for $C < 0$ (and $\alpha > -2$) the characteristics are both real and the system is hyperbolic. In this case, the problem simplifies dramatically and the KY model is similar to a modified shallow water model. There is a large body of work concerning the nature of the shallow water equations and so the hyperbolic case is not of primary interest. Equivalent but opposite classifications occur for the case $\alpha < -2$ which is not studied here.

2.6.3 Dispersion Relation

To better highlight the effect of the diffusion terms, the equations are linearized about an initial reference state with an infinitesimally small perturbation superimposed, i.e., $\underline{\phi} = \underline{\phi}_0 + \underline{\phi}'$. This solution is inserted into Eq. (2.100) and three assumptions are applied to greatly simplify the resulting equation: the initial reference state satisfies Eq. (2.100) automatically, products of perturbations are negligible and the reference state is either steady or the length scale of the reference state is considerably larger than that of the imposed perturbation, i.e., $\frac{\partial \phi_0}{\partial x} \ll \frac{\partial \phi'}{\partial x}$. The remaining terms define the linear perturbation equation,

$$\frac{\partial \phi'}{\partial t} + A_0 \frac{\partial \phi'}{\partial x} + \mathbf{D} \frac{\partial^2 \phi'}{\partial x^2} - \frac{\partial F_0}{\partial \underline{\phi}^{II}} \phi' = 0, \quad (2.103)$$

where A_0 and F_0 are evaluated at ϕ_0 . In typical fashion, the perturbation is assumed to be a traveling wave,

$$\underline{\phi}' = \hat{\phi}' e^{i(kx - \omega t)}, \quad (2.104)$$

where $\hat{\phi}'$ is the amplitude, k is the wavenumber, and ω is the angular frequency. The more intuitive variables of wavelength and frequency are related by $\lambda = 2\pi/k$ and $f = \omega/2\pi$, respectively. In general, the angular frequency may be complex and, from Eq. (2.104), when the imaginary component is positive the perturbation will grow exponentially in time. The real component of the angular frequency and the wavenumber defines the wave speed according to $c = \omega_R/k$.

Inserting Eq. (2.104) into Eq. (2.103) gives

$$\left(-i\omega + ikA_0 + (ik)^2 \mathbf{D} - \frac{\partial F_0}{\partial \underline{\phi}^{II}} \right) \phi' = 0. \quad (2.105)$$

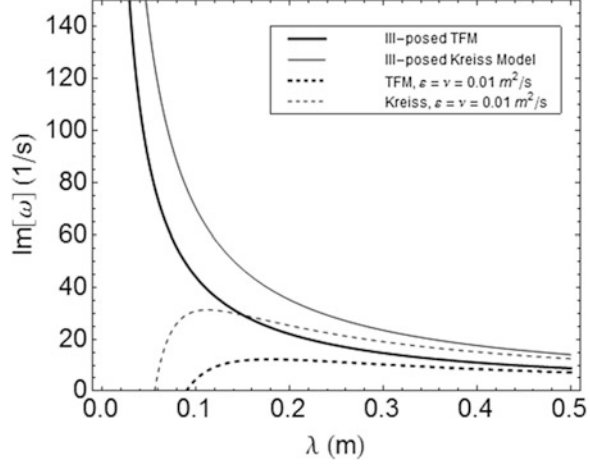
For a nontrivial solution to exist, the coefficient matrix of Eq. (2.105) must be singular, i.e.,

$$\det \left[\omega - kA_0 + ik^2 \mathbf{D} + i \frac{\partial F_0}{\partial \underline{\phi}^{II}} \right] = 0. \quad (2.106)$$

Solving Eq. (2.106) for the angular frequency gives

$$\omega = ku_0 - \frac{i}{2} \left[(\varepsilon + \nu)k^2 + 2 \pm \sqrt{((\varepsilon - \nu)k^2 + 2)^2 + (2c_{ik})^2} \right], \quad (2.107)$$

Fig. 2.18 Comparison of FFM and KY dispersion relations



where c_i is the imaginary component of the eigenvalues previously derived in Eq. (2.102). The larger imaginary root of the angular frequency is shown in Fig. 2.18 for a reference state of $\alpha_0 = u_0 = 1$ and $C = 1$. Consider the case $\varepsilon = \nu$:

$$\omega = uk - i\nu k^2 \pm k\sqrt{-C\left(1 + \frac{\alpha}{2}\right)}. \quad (2.108)$$

This dispersion relation is very similar to that of FFM equation (2.42) when $\varepsilon = \nu$ and $\sigma = 0$:

$$\omega = uk - i\nu k^2 \pm k\sqrt{-C\alpha}. \quad (2.109)$$

The model is ill-posed in the inviscid limit, i.e., $\varepsilon = \nu = 0$. Figure 2.18 shows the dispersion relations with $\alpha = 0.5$, $u = 1$ m/s, $C = 1$, and $\nu = 0, 0.01$ m/s² and the dynamic resemblance with Eqs. (2.37) and (2.38) becomes apparent.

It is readily seen from Eq. (2.108) that when diffusion is neglected, $\varepsilon = \nu = 0$, the growth rate, ω_i , will have a positive component indicating exponential growth. The ill-posed behavior is obvious: an infinitely short wavelength perturbation ($k \rightarrow \infty$) has an infinitely large growth rate ($\omega_i \rightarrow \infty$). For large k the growth rate is approximately linear with respect to k with a small, constant damping due to the source term. The linear growth rate is also seen in the 1D TFM under certain conditions and is a characteristic feature of the Kelvin–Helmholtz instability that is imbedded within the model equations.

If both viscosities are positive constants the linear stability changes even more dramatically, rather than approaching an asymptote the stability curve bends down and approaches negative infinity as $k \rightarrow \infty$. For the special case $\varepsilon = \nu$, the imaginary part of Eq. (2.107) reduces to three components: a negative constant component from the source term, a positive linear component from the underlying ill-posedness, and a quadratic negative term from the diffusion terms. The

combined result is that the growth rate is positive for a wavenumber range from $k \in (0, k_0)$ and negative for $k \in (k_0, \infty)$, as shown in Fig. 2.18. The value of the cut off wavenumber is given by $k_0 = \nu^{-1} \sqrt{c_i^2 - 2\nu}$. In the growth region there is a single maximum growth rate, the critical growth rate, given by $\omega_c = \frac{c_i^2}{4\nu} + \frac{\nu}{c_i^2} - 1$

which occurs at the critical wavenumber $k_c = \sqrt{\frac{c_i^2}{4\nu^2} - \frac{1}{c_i^2}}$. While there is still exponential growth, this type of linear instability is physically acceptable. Perturbations will grow if the wavelength is sufficiently long and decay at the short length scales. Lastly, it should be noted that the KY equations are not dispersive in any case since the real part of the angular frequency is always linear in k so that the wave speed is constant, i.e., $c = u$ (Whitham 1974).

The linear stability properties of the KY equations and how it is affected by the viscosities parallel that of the 1D TFM. In particular, to achieve a cutoff wavenumber with decay at short wavelengths, second-order diffusion terms must be added to all equations even when there is no physical justification. It is worth noting that both the 1D TFM and the KY equations can also be regularized with a combination of kinematic or turbulent viscosity and a third-order term related to surface tension. Such an approach introduces dispersion which increases the complexity of the problem and will not be explored here.

2.6.4 Method of Manufactured Solutions

The simplest way to test the code's correctness (errors or bugs) and accuracy (observed convergence rate) is to compare a numerical solution to a known exact analytical solution. Unfortunately the KY equations have no known solution that is sufficiently complex to exercise all of the terms. Certainly $\alpha(x, t) = 0$ and $u(x, t) = A$, where A is any constant, is a solution to Eqs. (2.98) and (2.99) but it provides no useful information for assessing the accuracy of the code (although such trivial solutions may be useful for checking the correctness of the code, i.e., debugging). Fortunately this problem has a clever remedy: simply manufacture a solution without being concerned about whether or not it exactly satisfies the governing PDEs. Then, if the manufactured solution does not exactly satisfy the governing PDEs, it is relatively straightforward to determine the residual source term that would modify the equations to make the manufactured solution an exact solution. This approach is often referred to as the method of manufactured solutions (MMS).

To begin, it helps to write of the KY equations as a pair of operators:

$$L_\alpha(\alpha, u) = \frac{\partial \alpha}{\partial t} + u \frac{\partial \alpha}{\partial x} + \left(1 + \frac{\alpha}{2}\right) \frac{\partial u}{\partial x} - \varepsilon \frac{\partial^2 \alpha}{\partial x^2} + 2\alpha \quad (2.110)$$

and

$$L_u(\alpha, u) = \frac{\partial u}{\partial t} + u \frac{\partial u}{\partial x} - C \frac{\partial \alpha}{\partial x} - \mu \frac{\partial^2 u}{\partial x^2}. \quad (2.111)$$

Then in operator form, the KY equations become $L_\alpha(\alpha, u) = L_u(\alpha, u) = 0$ for some $\alpha(x, t)$ and $u(x, t)$ that are exact solutions to Eqs. (2.98) and (2.99). Following Roache (1998), traveling waves are selected for the manufactured solutions:

$$\tilde{\alpha} = 2 + 0.5 \sin [\tilde{k}(x - \tilde{c}t)], \quad \tilde{u} = 1 + 0.5 \sin [\tilde{k}(x - \tilde{c}t)]. \quad (2.112)$$

The manufactured solutions are then inserted into the operators of Eqs. (2.100) and (2.101) giving

$$\begin{aligned} L_\alpha(\tilde{\alpha}, \tilde{u}) &= \tilde{k} \left(\frac{3}{2} - \frac{\tilde{c}}{2} \right) \cos [\tilde{k}(x - \tilde{c}t)] + \left(1 + \frac{\epsilon k^2}{2} \right) \sin [\tilde{k}(x - \tilde{c}t)] \\ &\quad + \tilde{k} \left(\frac{3}{16} \right) \sin [2\tilde{k}(x - \tilde{c}t)] + 4 = S_\alpha(x, t) \end{aligned} \quad (2.113)$$

and

$$\begin{aligned} L_u(\tilde{\alpha}, \tilde{u}) &= \left(\frac{\tilde{k}}{2} \right) \left(1 - \tilde{c} - C + \frac{1}{2} \sin [\tilde{k}(x - \tilde{c}t)] \right) \cos [\tilde{k}(x - \tilde{c}t)] \\ &\quad + \left(\frac{\nu \tilde{k}^2}{2} \right) \sin [\tilde{k}(x - \tilde{c}t)] = S_u(x, t) \end{aligned} \quad (2.114)$$

which define the source terms, $S_\alpha(x, t)$ and $S_u(x, t)$, necessary to modify the KY equations so that the manufactured solutions of Eq. (2.99) and (2.100) are exact solutions. The procedure could equivalently be called the method of manufactured equations since it is really the governing equations that are changed from their original form, $L_\phi(\alpha, u) = 0$, to a modified form, $L_\phi(\alpha, u) = S_\phi(x, t)$, to allow the handpicked solution to be an exact solution.

The source terms defined in Eqs. (2.113) and (2.114) are used as the sources in the finite difference functions in Eqs. (2.90) and (2.91) at discrete space locations x_i or x_j and time levels t^n . The initial conditions are given by the manufactured solutions at $t = 0$. Periodic boundary conditions are applied so that no special boundary values need to be determined from the manufactured solutions, but the domain or solution should be set so that there are an integer number of periods. The error between the code calculated solution and the manufactured exact solution will be assessed with a global L_2 norm defined by

$$e_2(\phi) = \frac{\sqrt{\sum_i^N (\phi_i - \tilde{\phi}(x_i))^2}}{\sqrt{\sum_i^N (\tilde{\phi}(x_i))^2}}. \quad (2.115)$$

The coarsest grid used for the MMS is $N = 25$ and the nodalization is successively doubled, i.e., Δx is halved, up to $N = 800$. The convergence rate between a grid N and the doubled grid $2N$ is given by

$$O = \frac{\ln \left[\frac{e_2(\phi_{2N})}{e_2(\phi_N)} \right]}{\ln \left[\frac{\Delta x_{2N}}{\Delta x_N} \right]} \quad (2.116)$$

which gives the order of accuracy of the code for grid sizes in the vicinity of $3N/2$. In the present work the grid refinement is always achieved by doubling the number of nodes so the denominator in Eq. (2.116) is simply $\ln(1/2)$. Additionally the time step should be refined consistently with the grid, which can be problematic since the time step is restricted by Δx^2 for small enough Δx . For each case the ratio $r_\Delta = \Delta t / \Delta x$ is set to a constant value so that the numerical stability condition of Eq. (2.97) is satisfied for all grids.

To begin, the simplest waveform is selected, i.e., $\tilde{k} = \tilde{c} = 1$ in Eq. (2.112), so that the solution is 2π -periodic in space and time. The domain is given by $x \in [-\pi, \pi]$ and the error will be assessed at $t = 2\pi$ to give one period in both space and time. The time step for each grid is set from the ratio $r_\Delta = \Delta t / \Delta x = 0.0125$. As may be somewhat expected, the MMS does not work and the calculated solution diverges from the manufactured solution. The traditional refinement plot or table are not shown because they offer little information. What is important to demonstrate is not simply that the solution diverges, but how it diverges.

The error for each variable is shown in Fig. 2.19 as a function of time for four different grids. (The two coarsest grids have been left out because the truncation error begins to affect the divergence rate.). The straight line in Fig. 2.19 beyond the finest grid is $e^{\omega_c(t-t^*)}$ with ω_c calculated using the average α of the exact solution

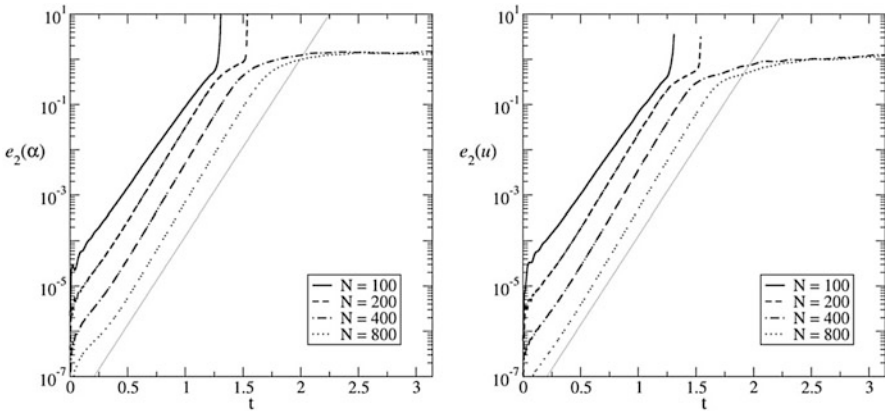


Fig. 2.19 Divergence of numerical method from the exact solution for the case $x \in [-\pi, \pi]$, straight line shows the average critical growth rate predicted from linear theory

and t^* is an arbitrary constant. This shows that for each case, there is an initial transient period after which the error grows exponentially and approximately uniformly at the critical growth rate. Beyond this period the solution either diverges to infinity (an excursion) or reaches an asymptotic value. A discussion on this difference is postponed to the end of Sect. 4.3.4.

Figure 2.18 shows that while the MMS did not work, it failed in a way that was predicted by the linear stability analysis of Sect. 2.6.3. Error is introduced to the calculation through two primary ways: round-off error in the finite precision representation of the source terms and truncation error by the finite difference representation of the differential equations. While these errors are initially very small, the linear stability analysis predicts that even infinitesimally small perturbations will grow exponentially in time. Therefore, some adjustments are needed in order to proceed with the code verification.

The most obvious change is to make the model hyperbolic, either by adjusting the model or adjusting the manufactured solution. This was tested by setting $C = -1$, which makes the model hyperbolic for the manufactured solution of the previous section, and convergence was indeed verified. However, this method of code verification raises several concerns, namely, that such an approach may not be applicable to other similar models, e.g., the 1D TFM.

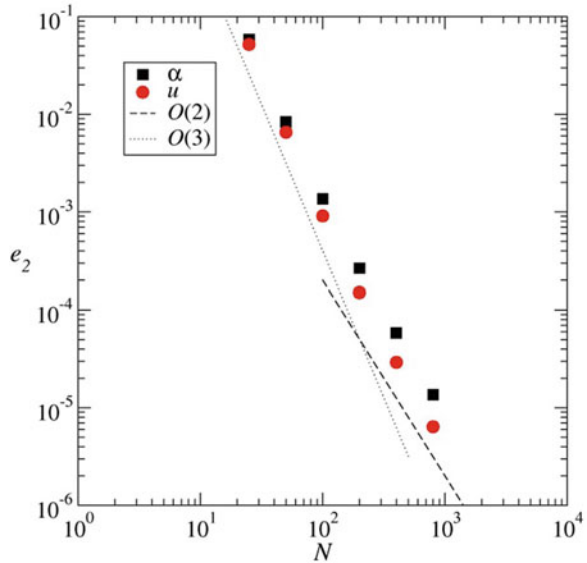
Without altering the form of the equations or the solution, there is one other option available: shrink the geometry of the problem so that domain simply cannot contain wavelengths with positive growth rate, i.e., $L \leq \lambda_0$. Using the maximum value of α in the manufactured solution, the maximum cutoff wavenumber is $k_0 = 20\sqrt{2.15} \cong 29.3$. Therefore, the domain will be reduced to $x \in [-\pi/30, \pi/30]$ so that the maximum possible wavelength is less than λ_0 and linear growth should not be possible. The wavenumber of the manufactured solution is modified to fit the new domain, $\tilde{k} = 30$, while the previous wave speed is retained, $\tilde{c} = 1$, so that the error is still assessed at one temporal period, $t = 2\pi$. The time step for each grid is set by $r_\Delta = \Delta t/\Delta x = 0.004$.

Now the error is reduced as the grid is refined. The error for each grid is shown in Table 2.1 and the convergent behavior is shown in Fig. 2.20. The convergence rate between two grids is also given in Table 2.1 which shows that the order of accuracy of the method is slightly better than second order. There is a noticeable convergence of the rate of convergence itself, which was also reported by others using the MMS (Burg and Murali 2006). For the coarsest grids the refinement brings almost third-

Table 2.1 Error and convergence rate between two successive grids for the case $x \in [-\pi/30, \pi/30]$

N	α		u	
	e_2	O	e_2	O
25	5.860E-02	—	5.187E-02	—
50	8.345E-03	2.81	6.568E-03	2.98
100	1.363E-03	2.61	9.103E-04	2.85
200	2.652E-04	2.36	1.501E-04	2.60
400	5.817E-05	2.19	2.925E-05	2.36
800	1.363E-05	2.09	6.410E-06	2.19

Fig. 2.20 Convergence rates for the second MMS case, $x \in [-\pi/30, \pi/30]$.



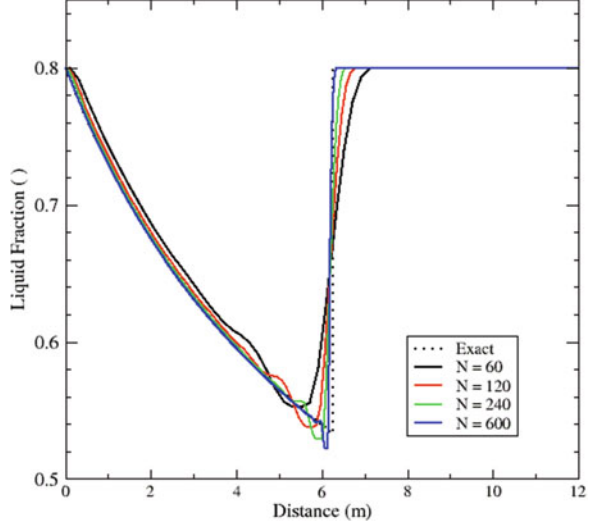
order accuracy, which is shown in Fig. 2.20 as the steeper initial line. However, as the grid is refined further the order of accuracy is reduced to near second order which is also shown in Fig. 2.20. It should be noted that this convergence rate is for smooth data (solutions) only. Discontinuous or piece-wise continuous solutions are discussed next.

Using such a small domain may not be physically relevant for some models, but this is not a concern of code verification. This provides a method to further distinguish ill-posed models from regularized models, since for an ill-posed model there will be no domain where the MMS is applicable. Lastly it should be pointed out that we are still left wondering whether or not the numerical method (and really any time marching scheme) is appropriate for this type of problem, but this is not really a question for the MMS or of code verification in general. With code verification one only wants to be sure that the code is working correctly, which has been shown.

2.6.5 Water Faucet Problem

The water faucet problem of Ransom (1984), derived in App. B.5.5, is a stable SWT case, i.e., $C = 0$, with a void jump. The purpose of this section is to verify the numerical FFM with the water faucet problem to assess the effect of a discontinuous solution. The uniform initial conditions are $\alpha_{10} = 0.8$ and $u_{10} = 10\text{m/s}$. The boundary conditions at the inlet are held constant at α_{10} and u_{10} . The SWT Eqs. (2.47) and (2.48) are solved analytically for $L = 12\text{m}$, $\rho_1 = 1000\text{kg/m}^3$, $\rho_2 = 1\text{kg/m}^3$, $C = 0$ and the source term $F = g$. The solution, derived in Appendix B.5.5, is

Fig. 2.21 Numerical solutions of the water faucet problem at $t = 0.5$ s with SSP2-SMART scheme



$$x < u_{10}t + \frac{1}{2}gt^2 \rightarrow \alpha_1(x, t) = \frac{\alpha_{10}u_{10}}{\sqrt{u_{10}^2 + 2gx}}, \quad u_1(x, t) = \sqrt{u_{10}^2 + 2gx} \quad (2.117)$$

or otherwise

$$\alpha_1(x, t) = \alpha_{10}, \quad u_1(x, t) = u_{10} + gt. \quad (2.118)$$

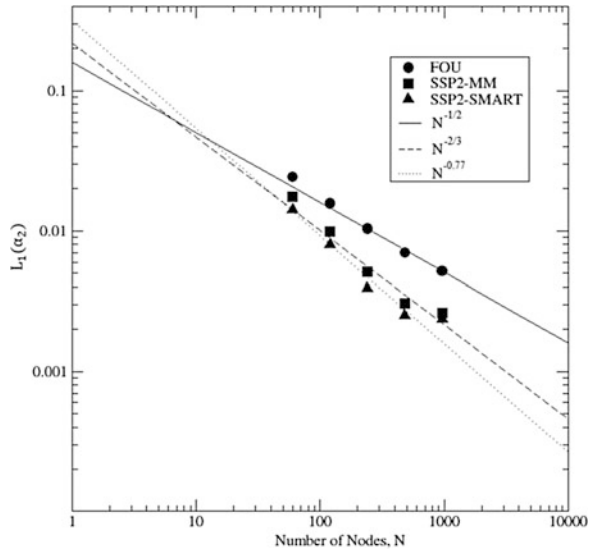
The second-order semi-implicit scheme of Sect. 2.5.5, including the SMART flux limiter, is verified in the presence of a contact discontinuity. The solutions are shown in Fig. 2.21 at $t = 0.5$ s for $Co = 0.5$. There is a small undershoot right before the shock, but otherwise the solution converges satisfactorily.

To quantify the convergence of two second-order schemes the L_1 error for the liquid fraction is calculated as

$$L_1(\alpha) = \frac{1}{N} \sum_{i=1}^N |\alpha_i - \alpha_{\text{exact}}(x_i)|. \quad (2.119)$$

The errors as a function of grid number are then fitted with a linear slope on a log-log plot to determine the global order of accuracy in Fig. 2.22. The convergence rates for both higher order schemes are significantly reduced, compared with the continuous case shown in Fig. 2.20. This reduction has been explained by Banks et al. (2008) for linearly degenerate waves. The convergence rates of the FOU, SSP2-MM, and SSP2-SMART schemes shown in Fig. 2.22 are extremely close to the theoretical L_1 errors of Banks et al. (2008), i.e., $O(\frac{1}{2})$ for FOU and $O(\frac{2}{3})$ for the SSP2-MM scheme. The SSP2-SMART scheme preforms slightly better, i.e., approximately $O(0.77)$.

Fig. 2.22 Convergence rates for three different schemes



Finally, it may be appropriate at this point to clarify why the linear theory of Banks et al. (2008) is applicable to the water faucet problem, which is a nonlinear problem. In the vicinity of the void jump, the velocity is continuous according to Eqs. (2.117) and (2.118), although it is discontinuous in the first derivative. Therefore, the velocities on either side of the jump are equal. Since the characteristics are given by the velocity, the jump speed is $u(x_d(t))$ and the water faucet problem describes a contact discontinuity (Lax 1972) which is linearly degenerate, unlike material shocks that have discontinuous velocities for $C > 0$, cf. Sect. B.5.3.

2.7 Kelvin–Helmholtz Instability

The purpose of this section is to show how the Kelvin–Helmholtz (KH) instability behaves in horizontal stratified flow for a well-posed FFM compared to an ill-posed one. The KH instability has been the subject of considerable research within the framework of the 1D TFM. Taitel and Dukler (1976) used it with linear stability theory to predict the flow regime transition from stratified to slug flow. In their simple interpretation, the 1D TFM becomes ill-posed at the transition as was shown in Sect. 2.4.1. However, Ramshaw and Trapp (1978) demonstrated that adding surface tension makes the model well-posed even when unstable. Very little work has been done on the nonlinear stability of the KH unstable TFM and since SWT does not contemplate the case $C > 0$ there are no equivalent analyses either. This topic is addressed in the next two chapters. The dynamically unstable TFM is therefore unique and exhibits, when the model is too incomplete, ill-posed behavior.

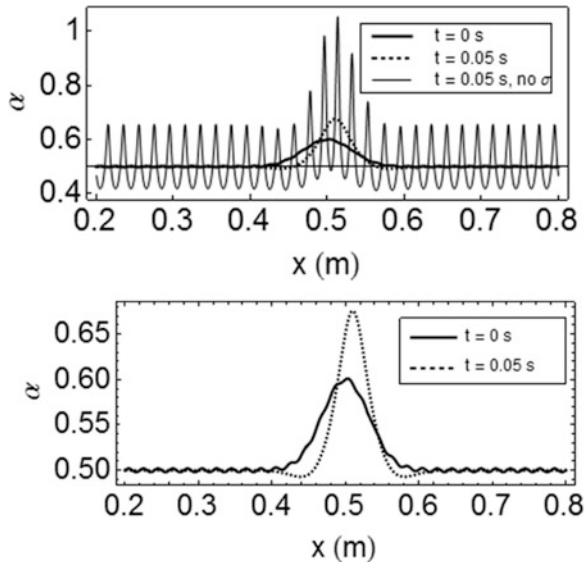
A “double wave” simulation, first introduced by Holmås et al. (2008), is considered here. The initial condition is a long wave of relatively large amplitude with a small amplitude high frequency, i.e., short wavelength, disturbance superimposed on top. The length scale of the short wave is arbitrary, i.e., 1 cm, but resembles that of capillary waves. A Gaussian is used for the large wave, instead of the single sine wave used by Holmås et al. (2008) which has a discontinuous derivative at both ends, namely:

$$\alpha_I(x, t = 0) = 0.5 + 0.1e^{-256(x-\frac{1}{2})^2} + 0.002 \sin\left(\frac{2\pi x}{0.01024}\right). \quad (2.120)$$

The simulation of the KH unstable FFM, Eqs. (2.37)–(2.38), is obtained for the initial near linear stage of wave growth with $\rho_1 = 1000 \text{ kg/m}^3$, $\rho_2 = 1 \text{ kg/m}^3$, $u_1 = 0.2 \text{ m/s}$, $C = 1$ (i.e., $u_2 - u_1 = 12.2 \text{ m/s}$), $\varepsilon = \nu = 0$, $F = 0$, $H = 0.15 \text{ m}$, with and without surface tension, i.e., $\sigma = 0.07 \text{ N/m}$ or 0 N/m . The boundary conditions are periodic. According to the dispersion analysis, the short-wavelength ripples will die out and the large wave will grow with time if the model is well-posed.

Figure 2.23 (bottom) shows the simulation of the FFM with surface tension (i.e., the well-posed problem). The high frequency wave is below the cutoff frequency predicted by the linear stability analysis and it is damped out while the large wave grows. On the other hand, Fig. 2.23 (top) shows that when surface tension is not included, i.e., the model is ill-posed, the high frequency wave has a larger growth rate and dominates the solution after a short time.

Fig. 2.23 Evolution of FFM wave with very short wavelength perturbation beyond KH threshold. *Thick solid line*: initial condition. *Dashed line*: well-posed, *thin solid line*: ill-posed



2.8 Summary and Discussion

The 1D TFM for horizontal or near-horizontal stratified flow has been simplified to the two-equation FFM to facilitate the local stability analyses of material waves. First, the incompressible assumption was applied to remove the acoustic waves, leaving only the material waves. Second, the fixed flux assumption removed the very long material wave instabilities. Finally the model was reduced to the SWT equations, in the limit $r_p \rightarrow 0$, which allows the well-known surface wave analysis of Whitham (1974) to be applied to the TFM. Two separate instabilities were identified, the dynamic KH instability and the kinematic SWT instability. Several results were obtained for these, using characteristic and dispersion analyses, under a unified treatment made possible by the simplified FFM equations.

The characteristic analysis shows that the FFM becomes ill-posed when the KH criterion is exceeded. This distinct KH-TFM condition arises because of the jump between the two-phase velocities and is not shared by single-phase flow models except for the exceptional multidimensional Euler vortex sheet problem. The dispersion analysis demonstrates that viscosity or surface tension, both of which stabilize the single-phase interface shear layer problem, make the TFM well-posed and in the process they stabilize it even though the shear layer physics is still absent. Furthermore, they change the nature of the material waves, in the case of viscosity, from hyperbolic to parabolic. Therefore, a well-posed TFM is hyperbolic–parabolic, like the Navier–Stokes equations. This linear result is both welcome and necessary but it is not sufficient, since the TFM must also be Lyapunov stable, i.e., wave growth must be bounded. In Chap. 4 we demonstrate Lyapunov stability with nonlinear simulations of a viscous 1D FFM that results in limit cycles and chaos.

The dispersion analysis also gives rise to the SWT instability of Whitham (1974) which occurs at a lower gas velocity and is used to predict the transition to wavy flow. An analytic expression for the stability boundary of stratified to wavy flow was derived from this condition. Finally the wave sheltering effect was incorporated into the model and good agreement was obtained with experimental data for the flow regime transition of Vallee et al. (2010).

The numerical stability of first-order finite difference schemes was analyzed with the von Neumann method. Even though these schemes have been well understood for a long time, their application presents a unique challenge when the TFM is ill-posed. It was found that while the FOU method may be used to regularize an ill-posed TFM, it also leads to nonconvergence in some cases. Furthermore, while the requirements that the scheme must be stable and nondispersive are easily met, too much stabilization may result not only in the desired dissipation of short waves but of long waves too, which may be detrimental.

A second-order scheme with a flux limiter was developed for a well-posed FFM. Its convergence was verified by the method of manufactured solutions (Roache 1998, 2002) and its capability to handle a contact discontinuity was verified with the water faucet problem. This numerical model is used throughout the book for the simulation of nonlinear behavior of the FFM. Finally a simulation was performed

with this model for the initial near linear stage of material wave growth caused by the KH instability. A comparison between a well-posed and an ill-posed FFM illustrates the initial near linear behavior under the ill-posed condition, while nonlinear simulations will be pursued in the next two chapters.

The stability analysis methods developed so far for the FFM will be applied to a full TFM in the next chapter.

References

- Anshus, B. E., & Goren, S. L. (1966). A method of getting approximate solutions to Orr–Sommerfeld equation for flow on a vertical wall. *AIChE Journal*, 12(5), 1004.
- Arai, M. (1980) Characteristics and Stability Analyses for Two-Phase Flow Equation Systems with Viscous Terms. *Nuclear Science and Engineering*, 74, 77–83.
- Banks, J. W., Aslam, T, and Rider, W. J. (2008) On sub-linear convergence for linearly degenerate waves in capturing schemes. *Journal of Computational Physics*, 227, 6985–7002.
- Barmak, I., Gelfgat, A., Ullmann, A., Brauner, N., & Vitoshkin, H. (2016). Stability of stratified two-phase flows in horizontal channels. *Physics of Fluids*, 28, 044101.
- Barnea, D., & Taitel, Y. (1993). Kelvin–Helmholtz stability criteria for stratified flow: Viscous versus non-viscous (inviscid) approaches. *International Journal of Multiphase Flow*, 19, 639–649.
- Barnea, D. & Taitel, Y. (1994) Interfacial and Structural Stability of Separated Flow. *International Journal of Multiphase Flow*, 20, 387–414
- Benjamin, T. B. (1959). Shearing flow over a wavy surface. *Journal of Fluid Mechanics*, 6, 161–205.
- Brauner, N., & Maron, D. M. (1993). The role of interfacial shear modelling in predicting the stability of stratified two-phase flow. *Chemical Engineering Science*, 48(16), 2867–2879.
- Burg, C. O. E., & Murali, V. K. (2006). The residual formulation of the method of manufactured solutions for computationally efficient solution verification. *International Journal of Fluid Dynamics*, 20(7), 521–532.
- Cohen, L. S., & Hanratty, T. J. (1965). Generation of waves in the concurrent flow of air and a liquid. *AIChE Journal*, 11(1), 138–144.
- Drazin, P. G., & Reid, W. H. (1981). *Hydrodynamic stability*. Cambridge: Cambridge University Press.
- Drew, D. A., & Passman, S. L. (1999). Theory of multicomponent fluids. In *Applied mathematical sciences*. Berlin: Springer.
- Drikakis, D., & Rider, W. (2005). *High resolution methods for incompressible and low-speed flows*. Berlin: Springer.
- Gaskell, P. H., & Lau, A. K. C. (1988). Curvature-compensated convective transport: SMART, a new boundedness-preserving transport algorithm. *International Journal for Numerical Methods in Fluids*, 8, 617–641.
- Gidaspow, D. (1974, September 3–7). Round table discussion (RT-1-2): Modeling of two-phase flow. In *Proceedings of 5th International Heat Transfer Conference*, Tokyo, Japan.
- Gottlieb, S., & Shu, C.-W. (1998). Total variation diminishing Runge-Kutta schemes. *Mathematics of Computation*, 67, 73–85.
- Henry, R. E., Grolmes, M. A., & Fauske, H. K. (1971). *Pressure-pulse propagation in two-phase one- and two-component mixtures*. Technical Report ANL-7792. Argonne National Laboratory.
- Holmås, H., Sira, T., Nordsveen, M., Langtangen, H. P., & Schulkes, R. (2008). Analysis of a 1D incompressible Two-Fluid model including artificial diffusion. *IMA Journal of Applied Mathematics*, 73, 651–667.

- Ishii, M., & Hibiki, T. (2006). *Thermo-fluid dynamics of two-phase flow* (1st ed.). New York: Springer.
- Keyfitz, B. L., Sever, M., & Zhang, F. (2004). Viscous singular shock structure for a non-hyperbolic Two-Fluid model. *Nonlinearity*, 17, 1731–1747.
- Kocamustafaogullari, G. (1985). Two-Fluid modeling in analyzing the interfacial stability of liquid film flows. *International Journal of Multiphase Flows*, 11, 63–89.
- Kreiss, H.-O., & Yström, J. (2002). Parabolic problems which are ill-posed in the zero dissipation limit. *Mathematical and Computer Modelling*, 35, 1271–1295.
- Kushnir, R., Segal, V., Ullmann, A., & Brauner, N. (2014). Inclined two-layered stratified channel flows: Long wave stability analysis of multiple solution regions. *International Journal of Multiphase Flow*, 62, 17–29.
- Lax, P. D. (1972) *Hyperbolic Systems of Conservation Laws and the Mathematical Theory of Shock Waves*, SIAM, Philadelphia, USA
- Lighthill, M. J., & Whitham, G. B. (1955). On kinematic waves I. Flood movement in long rivers. *Proceedings of Royal Society of London*, 229, 281.
- Lopez de Bertodano, M. A., Fullmer W., Vaidheeswaran, A. (2013) One-Dimensional Two-Equation Two-Fluid Model Stability. *Multiphase Science and Technology*, 25(2), 133–167.
- Oberkampf, W. L., & Roy, C. J. (2010). *Verification and validation in scientific computing*. Cambridge: Cambridge University Press.
- Oberkampf, W. L., Trucano, T. G., & Hirsch, C. (2004). Verification, validation and predictive capability in computational engineering and physics. *Applied Mechanics Reviews*, 57(5), 345–384.
- Ramshaw, J. D., & Trapp, J. A. (1978). Characteristics, stability and short wavelength phenomena in two-phase flow equation systems. *Nuclear Science and Engineering*, 66, 93–102.
- Ransom, V. H. (1984). Benchmark numerical tests. In G. F. Hewitt, J. M. Delhay, & N. Zuber (Eds.), *Multiphase science and technology*. Washington, DC: Hemisphere.
- Richtmeyer, R. D., & Morton, K. W. (1967). *Difference methods for initial-value problems* (2nd ed.). New York: Interscience.
- Roache, P. J. (1998). *Verification and validation in computational science and engineering*. Albuquerque: Hermosa.
- Roache, P. J. (2002). Code verification by the method of manufactured solutions. *Journal of Fluids Engineering*, 124, 4–10.
- Roe, P. L. (1986). Characteristic-based schemes for the Euler equations. *Annual Review of Fluid Mechanics*, 18, 337–365.
- Stadtke, H. (2006). *Gasdynamic aspects of two-phase flow: Hyperbolicity, wave propagation phenomena, and related numerical methods*. Weinheim, Germany: Wiley-VCH.
- Strang, G. (2007). *Computational science and engineering*. Wellesley, MA: Wellesley-Cambridge.
- Taitel, Y., & Dukler, A. E. (1976). A model for prediction of flow regime transitions in horizontal and near horizontal gas-liquid flow. *AIChE Journal*, 22, 47–55.
- Tannehill, J. C., Anderson, D. A., & Pletcher, R. H. (1997). *Computational fluid mechanics and heat transfer*. Washington, DC: Taylor & Francis.
- Tiselj, I., & Cerne, G. (2000). Some comments on the behavior of the RELAP5 numerical scheme at very small time steps. *Nuclear Science and Engineering*, 134, 306–311.
- Vallee, C., Lucas, D., Beyer, M., Pietruske, H., Schutz, P., & Carl, H. (2010). Experimental CFD grade data for stratified two-phase flows. *Nuclear Engineering and Design*, 240, 2347–2356.
- van Leer, B. (1979). Towards the ultimate conservative difference scheme. V. A second-order sequel to Godunov's method. *Journal of Computational Physics*, 32, 101–136.
- Wallis, G. B. (1969). *One-dimensional two-phase flow*. New York: McGraw-Hill.
- Waterson, N. P., & Deconinck, H. (2007). Design principles for bounded higher-order convection schemes—A unified approach. *Journal of Computational Physics*, 224, 182–207.
- Whitham, G. B. (1974). *Linear and nonlinear waves*. New York: Wiley.

Two-Fluid Model Stability, Simulation and Chaos

Bertodano, M.L. de; Fullmer, W.; Clausse, A.; Ransom, V.

2017, XX, 358 p. 74 illus., 60 illus. in color., Hardcover

ISBN: 978-3-319-44967-8